

## **Supplementary information**

---

# **Key role of chemistry versus bias in electrocatalytic oxygen evolution**

---

In the format provided by the authors and unedited

# Supplementary information for: Key role of chemistry versus bias in electrocatalytic oxygen evolution

Hong Nhan Nong<sup>1,2,7</sup>, Lorenz J. Falling<sup>3,7</sup>, Arno Bergmann<sup>4</sup>, Malte Klingenhof<sup>1</sup>, Hoang Phi Tran<sup>1</sup>, Camillo Spöri<sup>1</sup>, Rik Mom<sup>3</sup>, Janis Timoshenko<sup>4</sup>, Guido Zichittella<sup>5</sup>, Axel Knop-Gericke<sup>2,3</sup>, Simone Piccinin<sup>6</sup>, Javier Pérez-Ramírez<sup>5</sup>, Beatriz Roldan Cuenya<sup>4</sup>, Robert Schlögl<sup>2,3</sup>, Peter Strasser<sup>1</sup>, Detre Teschner<sup>2,3,†</sup> & Travis E. Jones<sup>3,†</sup>

<sup>1</sup>Department of Chemistry, Chemical and Materials Engineering Division, The Electrochemical Energy, Catalysis and Materials Science Laboratory, Technische Universität Berlin, Berlin, Germany.

<sup>2</sup>Department of Heterogeneous Reactions, Max-Planck-Institute for Chemical Energy Conversion, Mülheim an der Ruhr, Germany.

<sup>3</sup>Department of Inorganic Chemistry, Fritz-Haber-Institute of the Max-Planck-Society, Berlin, Germany.

<sup>4</sup>Department of Interface Science, Fritz-Haber-Institute of the Max-Planck-Society, Berlin, Germany.

<sup>5</sup>Institute for Chemical and Bioengineering, Department of Chemistry and Applied Biosciences, ETH Zurich, Zurich, Switzerland.

<sup>6</sup>Istituto Officina dei Materiali, Consiglio Nazionale delle Ricerche CNR-IOM, Trieste, Italy.

<sup>7</sup>These authors contributed equally: Hong Nhan Nong, Lorenz J. Falling.

†e-mail: teschner@fhi-berlin.mpg.de; trjones@fhi-berlin.mpg.de

## Contents:

### Materials and methods

<b>IrNi<sub>x</sub> precursor synthesis and electrode preparation</b>	<b>3</b>
<b>IrO<sub>x</sub> film preparation</b>	<b>3</b>
<b>IrO<sub>x</sub> Alfa Aesar-based electrode preparation</b>	<b>4</b>
<b>NiFe layered double hydroxide (LDH) preparation</b>	<b>4</b>
<b>Electrochemical setup</b>	<b>5</b>
<b>Electrochemical protocol</b>	<b>5</b>
<b>Outer and total capacitance</b>	<b>6</b>
<b>Impedance analysis</b>	<b>7</b>
<b>Operando Ir L-edge XAS sample preparation and setup</b>	<b>8</b>
<b>Operando O K-edge XAS sample preparation and setup</b>	<b>8</b>
<b>Halogen treatment</b>	<b>9</b>
<b>Surface area measurements</b>	<b>10</b>
<b>X-ray diffraction</b>	<b>10</b>
<b>X-ray photoelectron spectroscopy</b>	<b>11</b>
<b>Density functional theory</b>	<b>11</b>
<b>Supplementary Discussion</b>	
<b>Details of charge integration</b>	<b>13</b>

<b>Analysis of transient current response to voltage pulses</b>	<b>13</b>
<b>Ir L-edge details</b>	<b>27</b>
<b>O K-edge details</b>	<b>28</b>
<b><math>E_a</math> for <math>\mu_1</math>-OH deprotonation</b>	<b>30</b>
<b>Frumkin behavior</b>	<b>30</b>
<b><math>E_a</math> for <math>\mu_1</math>-OO coupling</b>	<b>32</b>
<b>Predicted OER current</b>	<b>33</b>
<b>NiFe LDH</b>	<b>34</b>
<b>Additional electrochemical assessments</b>	<b>34</b>
<b>Surface chlorination</b>	<b>36</b>
<b>Supplementary Tables</b>	
<b>Supplementary Table 1   Capacitance values of selected Ir samples</b>	<b>39</b>
<b>Supplementary Table 2   Areal capacitance values Alfa-Aeasar IrO<sub>x</sub></b>	<b>40</b>
<b>Supplementary Table 3   Samples and chlorination treatments</b>	<b>40</b>
<b>Supplementary Table 4   Charge values during pulse voltammetry</b>	<b>41</b>
<b>Supplementary Table 5   Cl<sub>2</sub> yield in Deacon reaction</b>	<b>41</b>
<b>Supplementary Table 6   XPS results on surface chlorination</b>	<b>42</b>
<b>Supplementary Table 7   Minimum energy path calculations summary</b>	<b>42</b>
<b>References</b>	<b>43</b>

## Materials and methods

### IrNi<sub>x</sub> precursor synthesis and electrode preparation

Synthesis of IrNi<sub>x</sub> bimetallic precursor alloy nanoparticles was performed according to polyol methods<sup>1,2</sup>. In brief, 0.122 g of Ni<sup>II</sup> acetate tetrahydrate (99.999%, Alfa Aesar), 0.156 g of 1,2-tetradecanediol (90%, Sigma Aldrich), 0.45 ml oleylamine (70%, Sigma Aldrich) and 0.45 ml oleic acid (99%, Alfa Aesar) were added to 30 ml dibenzyl ether ( $\geq 98\%$ , Sigma Aldrich) in a three-neck flask. The mixture was heated to 80 °C and maintained at this temperature for 30 min under stirring and nitrogen flow to remove trace water. The temperature was then increased to 240 °C, and 0.060 g of Ir(CH<sub>3</sub>COO)<sub>3</sub> ( $\geq 48\%$  wt. Ir, Chempur) was added. After 1 h, the reaction was allowed cool to room temperature.

Ti cylinders (10 mm diameter) were ground and polished to a mirror-like finish following Ref. <sup>3</sup>. In brief, the cylinders were first ground with SiC paper (Buehler), before grinding using ultra pad with diamond suspension (9  $\mu\text{m}$ , Buehler), and finally polishing using micro cloth with silica suspension (0.02  $\mu\text{m}$ , Buehler). The polished Ti cylinders were treated in 23% vol. HNO<sub>3</sub> at 80 °C for 2 h to remove impurities. Before use as catalyst substrates, the Ti cylinders were cleaned with ultrapure water and absolute ethanol.

3.335 mL of the synthesized IrNi<sub>x</sub> nanoparticles suspension was transferred into a 15 mL centrifuge tube. The nanoparticles were washed with absolute ethanol several times and collected by centrifugation at 6,000 revolutions per min (rpm) for 6 min. After this cleaning step the nanoparticles were re-dispersed in 1 mL of absolute ethanol by 10 min of sonification. 10  $\mu\text{L}$  of nanoparticle suspension was drop-casted on both pre-polished and cleaned Ti and glassy carbon (GC) cylinders (10 mm diameter) and was air dried at room temperature. Both sample types were annealed in 4% vol. H<sub>2</sub>/Ar at 400 °C for 1 h. The samples are denoted IrNi/Ti and IrNi/GC.

For quantification, 400  $\mu\text{L}$  of the nanoparticle suspension was transferred to a quartz tube. The nanoparticles were dried and dissolved with a mixture of aqua regia and NaClO<sub>3</sub> (Alfa Aesar) using a microwave to determine Ir content using ICP-OES. 9.7  $\mu\text{g}_{\text{Ir}}$  was loaded on the cylinders.

### IrO<sub>x</sub> film preparation

Thin Ir precursor films were applied onto polished cleaned Ti cylinders by spin coating (WS-650MZ-23NPP, Laurell). 40  $\mu\text{L}$  of coating solution (80 g L<sup>-1</sup> Ir<sup>III</sup> acetate,

99.95%, Chempur in absolute ethanol) was applied on the spinning cylinder at 200 rpm ensuring full coverage. The rotation velocity was increased to 2,000 rpm (200 revolution s<sup>-2</sup>), where it was dwelled for 45 s. The coated cylinders were annealed in a preheated muffle furnace (Carbolite) at 250 °C for 15 min. The samples are denoted IrO<sub>x</sub>/Ti-250°C. A similar spin coating procedure, using 40 g L<sup>-1</sup> Ir<sup>III</sup> acetate solution and 450 °C annealing, was performed to obtain IrO<sub>2</sub>/Ti-450°C.

To determine the Ir loading on the cylinders, uncalcined films were dissolved in 10 mL of water. The Ir concentrations in the solutions were measured by ICP-OES. The Ir loadings in IrO<sub>x</sub>/Ti-250°C and IrO<sub>2</sub>/Ti-450°C were 64.2 μg<sub>Ir</sub> and 31.1 μg<sub>Ir</sub>, respectively.

#### **IrO<sub>x</sub> Alfa Aesar-based electrode preparation**

IrO<sub>x</sub> powder (CAS: 12030-49-8) was sourced from Alfa-Aesar (Premion™, 99.99%, metals basis). To prepare the working electrodes, 5 mg of catalyst was suspended in 3,980 μL ultrapure water (Millipore, 18 MΩ), 1,000 μL isopropanol and 20 μL Nafion solution (5 wt %) before 20 min horn sonication to form a uniform ink. 10 μL of the ink was pipetted onto a pre-polished and cleaned glassy carbon rotating disk electrode (RDE, 5 mm diameter, Pine Instrument) and air dried at 60 °C for 9 min, resulting in a thin catalyst film. Based on the pipetted volume, 10 μg<sub>IrO<sub>x</sub></sub> was on the GC electrode.

#### **NiFe layered double hydroxide (LDH) preparation**

NiFe-LDH was prepared through a microwave assisted autoclave synthesis. For the preparation, 1,200 μL (0.6 M) Ni(OAc)<sub>2</sub>\*4H<sub>2</sub>O (Sigma Aldrich, 99.99% purity) and 240 μL (0.6 M) Fe(NO<sub>3</sub>)<sub>3</sub>\*9H<sub>2</sub>O (Alfa Aesar, 98% purity) were mixed. 6 mL dimethylformamid (DMF, Carlo Erba Reagents) was added to the precursor solution and the mixture was stirred for 2 h. 4 mL DMF and 8 mL ultrapure water (18.2 MΩ) were added before a two-step (60 min at 120 °C and 30 min at 160 °C) microwave treatment. The product was collected via centrifugation, washed with ethanol and ultrapure water followed by lyophilization.

To prepare the working electrodes, 4 mg NiFe-LDH was suspended in 768 μL ultrapure water (18.2 MΩ), 200 μL i-PrOH and 32 μL Nafion (5 wt %) followed by 15 min horn sonication. 10 μL of this ink was pipetted on a pre-cleaned and polished glassy carbon RDE (5 mm diameter, Pine Instruments) and dried at 55 °C for 10 min. 40 μg<sub>NiFe-LDH</sub> was on the GC.

### Electrochemical setup

Electrochemical experiments were performed in a three-compartment glass H cell with a RDE (Pine Instrument) and a potentiostat (Biologic) at room temperature. A Pt-mesh counter electrode was used. A reference Hg/Hg<sub>2</sub>SO<sub>4</sub> (MMS) electrode (in saturated K<sub>2</sub>SO<sub>4</sub>) and a hydrogen electrode (HydroFlex®) were used in 0.05M H<sub>2</sub>SO<sub>4</sub> and 0.1M KOH, respectively. The MMS and HydroFlex® electrodes were calibrated against the RHE before electrochemical measurements in the corresponding H<sub>2</sub>-saturated electrolytes. All electrochemical measurements of Ir-based catalysts were carried out in N<sub>2</sub>-saturated 0.05 M H<sub>2</sub>SO<sub>4</sub> and repeated with two to three electrodes for each catalyst. Unless otherwise noted, each presented dataset corresponds to an experiment using a single representative electrode.

### Electrochemical protocol

Electrocatalytic OER activities were recorded by sweeping the potential from 1.0 V to 1.8 V and back (5 mV s<sup>-1</sup>) with 1,600 rpm electrode rotation. PEIS (Potentiostatic Electrochemical Impedance Spectroscopy) was carried out before each OER measurement for *iR*-correction. The Ir-mass based OER activity was evaluated as the current normalized to the IrO<sub>2</sub> mass on the electrode with *iR*-corrected potential.

Before the OER scan, an activation step including 1 CV between 1.0 V and 1.8 V and 50 cycles between 0.05 V and 1.5 V was applied for the IrNi samples to leach out Ni<sup>2+</sup>. For other samples this activation step was skipped. After the OER scan, three CVs (0.4 V to 1.4 V) were performed, followed by a series of CVs between 0.93 V and 1.03 V (for IrO<sub>x</sub>/Ti-250°C and IrO<sub>2</sub>/Ti-450°C) or between 1.1 V and 1.2 V (for IrNi/Ti) with different scan rates, (2, 5, 10, 25, 50, 75, 100, 125, 150, 175, 200, 250, and 300) mV s<sup>-1</sup>, for the determination of outer and total charge<sup>4</sup>. All CVs were measured without electrode rotation; all other techniques, including Pulse voltammetry (PV), were measured with 1,600 rpm rotation.

Pulse voltammetry (PV) were performed while following current over time (1,600 rpm RDE). The potential was kept at a low potential ( $E_l = 1.35$  V) for 4 s, then switched and kept at a higher potential ( $E_h$ ) for 5 s before returning to  $E_l$  for 4 s. This cycle was repeated while increasing  $E_h$  from 1.42 V to 1.80 V in 20 mV/step and keep  $E_l$  unchanged. The current was sampled at every 0.0002 s (and 0.001 s) for the cathodic (anodic) sections. The OER current was read at the end of the 5 s anodic potential segment. Another PV protocol applied a broad potential window,  $E_l = 0.748$

V and  $0.948 \text{ V} \leq E_h \leq 1.698 \text{ V}$ , holding 15 s at each potential with 0.002 s current sampling. For the above experiments, a relatively high surface area counter electrode was placed in the same compartment as the working electrode to avoid the current being limited by the counter electrode. Rotation speed dependent (800 rpm to 2,000 rpm) pulse measurements on  $\text{IrO}_x/\text{Ti}$ -250°C indicate the result's independence to rotation speeds (see supplementary discussion section: Additional electrochemical assessments). Charge related to the potential step was calculated by integrating the current pulse over time accounting for the background current signal. The PV protocol for NiFe-LDH was identical except in 0.1M KOH (Sigma-Aldrich, 99.99%) and  $E_1 = 1.5 \text{ V}$ .

#### Outer and total capacitance

According to Trasatti *et al.*<sup>4,5</sup>, total charge ( $q^*_{\text{T}}$ ) which is proportional to the whole active surface and outer charge ( $q^*_{\text{O}}$ ), which is related to the “outer” surface of metal oxides and directly accessible to proton exchange, can be evaluated based on voltammetric charge at different scan rates. The relationship between  $q^*_{\text{T}}$  and scan rate  $\nu$  has been found to be<sup>4,5</sup>:

$$\frac{1}{q^*(\nu)} = \frac{1}{q^*_{\text{T}}} + k_1 \nu^{1/2} \quad . \quad (\text{Supplementary Eq. 1})$$

By plotting the reciprocal of  $q^*$  against  $\sqrt{\nu}$  and extrapolating the linear fit toward  $\nu = 0$  mV/s, the intercept can be considered as the reciprocal of  $q^*_{\text{T}}$ .

The relationship between  $q^*_{\text{O}}$  and scan rate has been found to be<sup>4,5</sup>:

$$q^*(\nu) = q^*_{\text{O}} + k_2 \nu^{-1/2} \quad . \quad (\text{Supplementary Eq. 2})$$

By plotting  $q^*$  against the reciprocal of the square root of the scan rate and extrapolating the linear fit toward  $\nu = \infty$ , the intercept can be considered as the  $q^*_{\text{O}}$ . Instead of using voltammetric charge, whose values depend on the potential range, interfacial capacitance can be used<sup>6</sup>. The interfacial capacitance ( $C$ ) can be evaluated according to the following equation:

$$C = \frac{\int_{E_1}^{E_2} i_{\alpha} dE + \int_{E_2}^{E_1} |i_c| dE}{2\nu(E_2 - E_1)} \quad , \quad (\text{Supplementary Eq. 3})$$

Where  $i_a$  and  $i_c$  are the instantaneous anodic and cathodic current, respectively,  $E_1$  and  $E_2$  are the cutoff potentials in the CVs.

By definition, the relationship between interfacial capacitance and the voltammetric charge is:

$$C(v) = \frac{q^*(v)}{E_2 - E_1}, \quad (\text{Supplementary Eq. 4})$$

Therefore, in analogue to  $q^*_T$  and  $q^*_O$ , total capacitance  $C_T$  and outer capacitance  $C_O$  can be determined based on the following equations:

$$\frac{1}{C(v)} = \frac{1}{C_T} + k'_1 v^{1/2} \quad (\text{Supplementary Eq. 5})$$

and

$$C(v) = C^*_O + k'_2 v^{-1/2}. \quad (\text{Supplementary Eq. 6})$$

Voltammograms at differing scan rates and evaluation of outer/total capacitance based on scan-rate experiments are shown in supplementary discussion section: Additional electrochemical assessments.

#### Impedance analysis

Following the above protocol, potentiostatic electrochemical impedance spectroscopy (PEIS) measurements were performed from 0.4 V to 1.4 V. An equivalent circuit consisted of  $L1R1(Q2R2)(Q3R3)$  was used to fit the PEIS spectra, where  $L1$ ,  $R1$ ,  $R2$ , and  $R3$  symbolize the inductance, the ohmic resistance of the electrolyte, the charge transfer resistance, and the catalyst film resistance, respectively<sup>6,7</sup>. The  $Q2$  and  $Q3$  are the so-called Constant Phase Elements (CPE), whose impedance is described by the formula<sup>7</sup>:

$$Z_{\text{CPE}} = \frac{1}{B(i\omega)^\alpha}, \quad (\text{Supplementary Eq. 7})$$

where  $B$  is a frequency independent term with units of ( $F s^{\alpha-1}$ ),  $\omega$  is the angular velocity and  $i=(-1)^{1/2}$ . The  $(Q2R2)$  parallel combination represents the charge transfer resistance of a faradaic process occurring at the catalyst/electrolyte interface, whereas the  $(Q3R3)$  combination represents the diffusion/adsorption of reaction intermediates<sup>7,8</sup>. Here the  $Q2$  includes both the double layer capacitance and the

pseudocapacitance. The corresponding effective capacitance  $C_{\text{eff},2}$  can be calculated according to the equation<sup>6,9</sup>:

$$C_{\text{eff},2} = Q_2^{\frac{1}{\alpha_2}} \left( \frac{1}{R_1} + \frac{1}{R_2 + R_3} \right)^{\frac{\alpha_2 - 1}{\alpha_2}} \quad (\text{Supplementary Eq. 8})$$

The effective capacitance ( $C_{\text{eff},2}$ ) values at different electrode potentials and examples of experimental Nyquist plots and corresponding fits are presented in the supplementary discussion section: Additional electrochemical assessments.

#### **Operando Ir L-edge XAS sample preparation and spectroscopy setup**

IrO<sub>x</sub> thin film on 10 μm Ti foil was prepared using an approach similar to IrO<sub>x</sub>/Ti-250°C by using ~160 g L<sup>-1</sup> Ir (III) acetate solution previously described. The solution was filtered by syringe filter (Nylon, 0.2 μm) before use. The sample was annealed at 250 °C in air for 5 min, followed by another spin coating step and finally annealed at 250 °C for 15 min.

Fluorescence yield (FY) operando XAS were recorded at beamline P64 of Petra III using a Si(111) double crystal monochromator and a PIPS detector measuring FY through the backside of the Ti foil substrate with the sample normal oriented 45° with respect to the X-ray beam and detector. The energy was calibrated using an IrO<sub>2</sub> reference. Ir L<sub>3</sub> and L<sub>2</sub> spectra were recorded in one scan using 0.05M H<sub>2</sub>SO<sub>4</sub> electrolyte, Pt mesh counter electrode and an Ag/AgCl (sat. KCl) reference electrode. Ohmic resistance was determined using the current interrupt method of the Biologic SP-200 potentiostat. Individual results are from single experiments.

#### **Operando O K-edge XAS sample preparation and spectroscopy setup**

11 mm Nafion disks (Nafion N117, The Chemours Company) were used as supports for Ir-based electrocatalysts, which were covered in Graphene obtained by Cu etching of 6x6 mm single layer graphene on Cu (Graphenea San Sebastian, Spain) in etching solution with 10 g of (NH<sub>4</sub>)<sub>2</sub>SO<sub>4</sub> (Merck, Darmstadt, Germany) in 250 mL MilliQ water for 12 h.

Nafion membranes for IrNi deposition were sputtered with ca. 1.4 nm carbon before electrophoretic deposition of IrNi NPs: 8 μL of NP suspension was pipetted onto the membrane before applying 2 V to the membrane (working electrode) for 75

min. Afterwards, the membranes were rinsed with absolute ethanol and washed with water. Graphene sheets (after Cu etching) were transferred onto the membranes. IrO<sub>x</sub> thin-film on graphene/Cu was prepared by spin coating and calcination. 60 μL 5 g L<sup>-1</sup> Ir (III) acetate was pipetted on the graphene/Cu foil (~12x12 mm) at 200 rpm before increasing to 6,000 rpm (200 revolution s<sup>-2</sup>) and dwelled for 45 s. The samples were annealed at 250 °C in air for 15 min. This IrO<sub>x</sub>/graphene/Cu foil was cut to ~6x6 mm and underwent 12 h Cu etching before transferring the IrO<sub>x</sub>/graphene sheets to Nafion membranes.

Operando O K-edge measurements were performed at the ISIS beamline (BESSY II) NAP-XPS end station using the in situ cell described in<sup>10</sup>. The equilibrium pressure in the chamber ( $5.0 \times 10^{-2}$  mbar to  $1.5 \times 10^{-1}$  mbar) was a balance between evaporation from the in situ cell and pumping via the 1 mm nozzle to the analyzer. For potentiodynamic PV, H<sub>2</sub>O<sub>gas</sub> was dosed to maintain  $2.5 \times 10^{-1}$  mbar and facilitate constant XA over time. O K-edge spectra were recorded in total (TEY) and partial electron yield (PEY). TEY was collected through the nozzle using a bias of 90 V against the working electrode and was used for steady-state spectra (0.05 eV steps, 0.2 s dwell time). Energy alignment was done by setting the H<sub>2</sub>O<sub>gas</sub> 3p-Rydberg state to 537.2 eV. Spectra were normalized to the maximum intensity at ~538 eV after removing the gas-phase signal. For potentiodynamic PV the PEY at 529 eV (collecting electrons with 385 eV kinetic energy in the analyzer, pass energy 100 eV) was followed during the PV protocol:  $E_1 = 0.75$  (or 1.1) V,  $0.95 \text{ V} \leq E_h \leq 1.7 \text{ V}$  with 15 s holding time. Each steady-state O K-edge spectrum was measured on a previously non-beam-exposed spot. Individual results are from single experiments.

World Precision Instruments (Sarasota, USA) Ag/AgCl reference electrodes (type DRIREF-2SH, stored in saturated KCl solution) were used with a Pt wire counter electrode and 0.05 M H<sub>2</sub>SO<sub>4</sub> electrolyte (0.5 mL min<sup>-1</sup> to the rear of the membrane). A boron-doped diamond lid pressed the membrane onto the cell body. The counter, reference, and working electrode were connected to a SP-300 potentiostat (Biologic) operated in floating mode. The working electrode was grounded to the electron analyzer. The Ag/AgCl reference electrode was calibrated against RHE after electrochemical measurements in H<sub>2</sub>-saturated 0.05 M H<sub>2</sub>SO<sub>4</sub>.

### Halogen treatment

The halogen-based treatments conducted on Alfa-Aesar IrO<sub>x</sub> samples were performed at ambient pressure in a continuous-flow fixed-bed reactor described elsewhere<sup>11</sup>. Briefly, the gases: HCl (Air Liquide, purity 2.8, anhydrous), O<sub>2</sub> (PanGas, purity 5.0), Cl<sub>2</sub> (Pan Gas, purity 2.8), and He (PanGas, purity 5.0; carrier gas) were fed using digital mass-flow controllers (Bronkhorst<sup>®</sup>) to the mixing unit equipped with a pressure indicator. A quartz reactor (internal diameter,  $d_i = 8$  mm) was loaded with sample ( $W_{\text{samp}} = 0.25$  g), and placed in a homemade electrical oven. Prior to testing, the bed was heated under He flow to the desired temperature ( $T = 298$  K to 723 K) and stabilized for  $\geq 30$  min before the gaseous mixture was fed at the desired space velocity ( $F_T:W_{\text{samp}} = 40$  L STP h<sup>-1</sup> g<sub>samp</sub><sup>-1</sup>) and feed composition (see Supplementary Table 3 in Supplementary tables section). All treatments were conducted with a holding time ( $t_h$ ) of 1.5 h, unless specified otherwise. Prior to any chlorination treatment, excluding Deacon, all IrO<sub>x</sub> samples were pre-calcined in static air at 723 K for 1 h with a heating ramp of 5 K min<sup>-1</sup>. After the treatments, the reactor was quenched to room temperature in He flow and the sample was retrieved for *ex situ* characterization and OER assessment.

Quantification of Cl<sub>2</sub> at the reactor outlet after the Deacon reaction (HCl + O<sub>2</sub>) was performed by its absorption in an impinging bottle filled with 0.1 M KI solution (Cl<sub>2</sub> + 3I<sup>-</sup> → I<sub>3</sub><sup>-</sup> + 2Cl<sup>-</sup>) followed by iodometric titration (Mettler Toledo G20 Compact Titrator) of the formed triiodide (I<sub>3</sub><sup>-</sup> + 2S<sub>2</sub>O<sub>3</sub><sup>2-</sup> → 3I<sup>-</sup> + S<sub>4</sub>O<sub>6</sub><sup>2-</sup>) with 0.01 M sodium thiosulfate solution (Aldrich, 99.99%). The activity data collected are summarized in Supplementary Table 5 in the Supplementary tables section.

### Surface area measurements

Catalyst surface areas were determined using a volumetric physisorption apparatus (Autosorb-6-B, Quantachrome). The catalysts were treated in a dynamic vacuum at 423 K for 2.4 h prior to Kr adsorption at 77 K. Surface area was calculated using the BET method in the pressure range  $p/p_0 = 0.05$ – $0.3$  with 11 data points. The reported values are the results of single experiments on each material.

### X-ray diffraction

XRD measurements were performed in Bragg–Brentano geometry on a Bruker AXS D8 Advance II theta/theta diffractometer, using Ni filtered Cu K $\alpha$  radiation and a

position sensitive LynxEye silicon strip detector and on a STOE STADI P transmission diffractometer equipped with a primary focusing germanium monochromator (Cu K $\alpha$ \_1 radiation) and DECTRIS MYTHEN 1K position sensitive solid-state detector. The reported diffractograms are the results of single experiments on each material.

#### **X-ray photoelectron spectroscopy**

The Cl 2p (and Cl/Ir ratio) of the chlorination series samples were analyzed by X-ray photoelectron spectroscopy (XPS). Powder samples (pressed into pellets) were measured at the BEIChem beamline (BESSY II) using  $h\nu = 415$  eV. Quantification was based on theoretical cross sections with asymmetry parameter correction from Yeh and Lindau<sup>12</sup> assuming differences in the inelastic mean free path and transmission function of the spectrometer for the Ir 4f and Cl 2p photoelectrons approximately cancel. Systematic error from this assumption will not change the Cl/Ir ratio order of the samples.

An electrode sample, based on catalysts films (AA-D) on GC disks before and after OER tests was analyzed by laboratory XPS (non-monochromatized Al K $\alpha$  (1,486.6 eV) excitation and a hemispherical analyzer (Phoibos 150, SPECS)). The results show OER changes the Cl/Ir ratio by only 10%. All reported values are the results of single experiments on each material.

#### **Density functional theory**

Spin polarized DFT calculations were performed with the Quantum ESPRESSO package version 6.4.1 using the PBE exchange and correlation potential<sup>13</sup>.

Pseudopotentials were chosen from the standard solid-state pseudopotentials database (SSSP Efficiency)<sup>14</sup>; for Ir, several pseudopotentials show similar test results and the projected augmented wave dataset from the PSLibrary<sup>15</sup> was used rather than the standard SSSP pseudopotential. A wave function cutoff of 60 Ry and a charge density cutoff of 540 Ry was used. Surface phase diagrams were computed using symmetric 4-layer (1 $\times$ 2) (110) rutile-type IrO<sub>2</sub> slabs separated by 18 H<sub>2</sub>O by considering five surface terminations: i)  $\mu_2$ -OH/ $\mu_2$ -OH and  $\mu_1$ -OH/ $\mu_1$ -OH; ii)  $\mu_2$ -O/ $\mu_2$ -OH and  $\mu_1$ -OH/ $\mu_1$ -OH; iii)  $\mu_2$ -O/ $\mu_2$ -O and  $\mu_1$ -OH/ $\mu_1$ -OH; iv)  $\mu_2$ -O/ $\mu_2$ -O and  $\mu_1$ -O/ $\mu_1$ -OH; v)  $\mu_2$ -O/ $\mu_2$ -O and  $\mu_1$ -O/ $\mu_1$ -O, see supplementary discussion section: Frumkin behavior. Each surface was equilibrated in water for  $\sim 5$  ps using a 1 fs timestep at 350

K (to account for the PBE induced over structuring of water). A Berendsen thermostat controlled the ionic temperature ( $dt/\tau = 1/50$ ) and a  $2 \times 2$   $k$ -point mesh was used with Marzari-Vanderbilt smearing ( $\sigma = 0.02$  Ry)<sup>16</sup>. The surface  $E$  vs. pH phase diagram was generated with the computational hydrogen electrode<sup>17</sup>, including configurational entropy for equivalent adsorption sites and zero-point energies for  $\mu_1$ -OH and  $\mu_2$ -OH from calculations on surfaces relaxed in vacuum, by taking random snapshots from the last ps of the MD simulations. This allows reduction of error in the bulk water<sup>18</sup> contribution to interfacial energy<sup>19</sup>:

$$\langle E_{\text{int}} \rangle = \frac{1}{2N} \left( \sum_{i=1}^N E_{\text{tot}} - \sum_{i=1}^N E_{\text{H}_2\text{O}} - \sum_{i=1}^N E_{\text{surf}} \right), \quad (\text{Supplementary Eq. 9})$$

where the  $1/2$  accounts for the slab's two sides,  $N$  is the number of snapshots,  $E_{\text{tot}}$  is the total energy of the solvated slab,  $E_{\text{H}_2\text{O}}$ , the energy of the water, and  $E_{\text{surf}}$  the energy of the slab without water, all computed with a  $4 \times 4$   $k$ -point mesh.  $\langle E_{\text{int}} \rangle$  was added to the average  $E_{\text{surf}}$ . Snapshots were included until energy convergence was better than 0.1 eV (8-32 snapshots per hydrogen coverage). The phase diagram was computed by interpolating between the computed hydrogen coverages using a quadratic function to capture the Frumkin behavior, see supplementary discussion section: Frumkin behavior and Supplementary Fig. 14, and is similar to that found using ice-like solvent<sup>20</sup>, though spread over a wide potential window.

Minimum energy paths were computed by starting with an MD snapshot of the  $\mu_2$ -O/ $\mu_2$ -O and  $\mu_1$ -O/ $\mu_1$ -OH and retaining 2 water bilayers on one surface while introducing  $\sim 15$  Å of vacuum to separate periodic images.  $\mu_1$ -OH was removed from the non-solvated side and the bottom two layers of atoms were fixed to their bulk coordinates. Fixed charge calculations had zero net charge in the simulation cell. Fixed bias calculations used the effective screening medium method<sup>21,22</sup> at pzc and 0.1 V to 0.5 V anodic of it. Transition states were found by climbing image nudged elastic band while allowing the initial states to relax. This process was repeated for all surface terminations using a  $4 \times 4$   $k$ -point (a 4-layer ( $2 \times 4$ ) cell ( $2/8$   $\mu_1$ -OH) using a  $2 \times 2$   $k$ -point mesh was also used). The paths were considered converged when the force on each image was below 0.05 eV/Å.

## Supplementary Discussion

### Details of charge integration

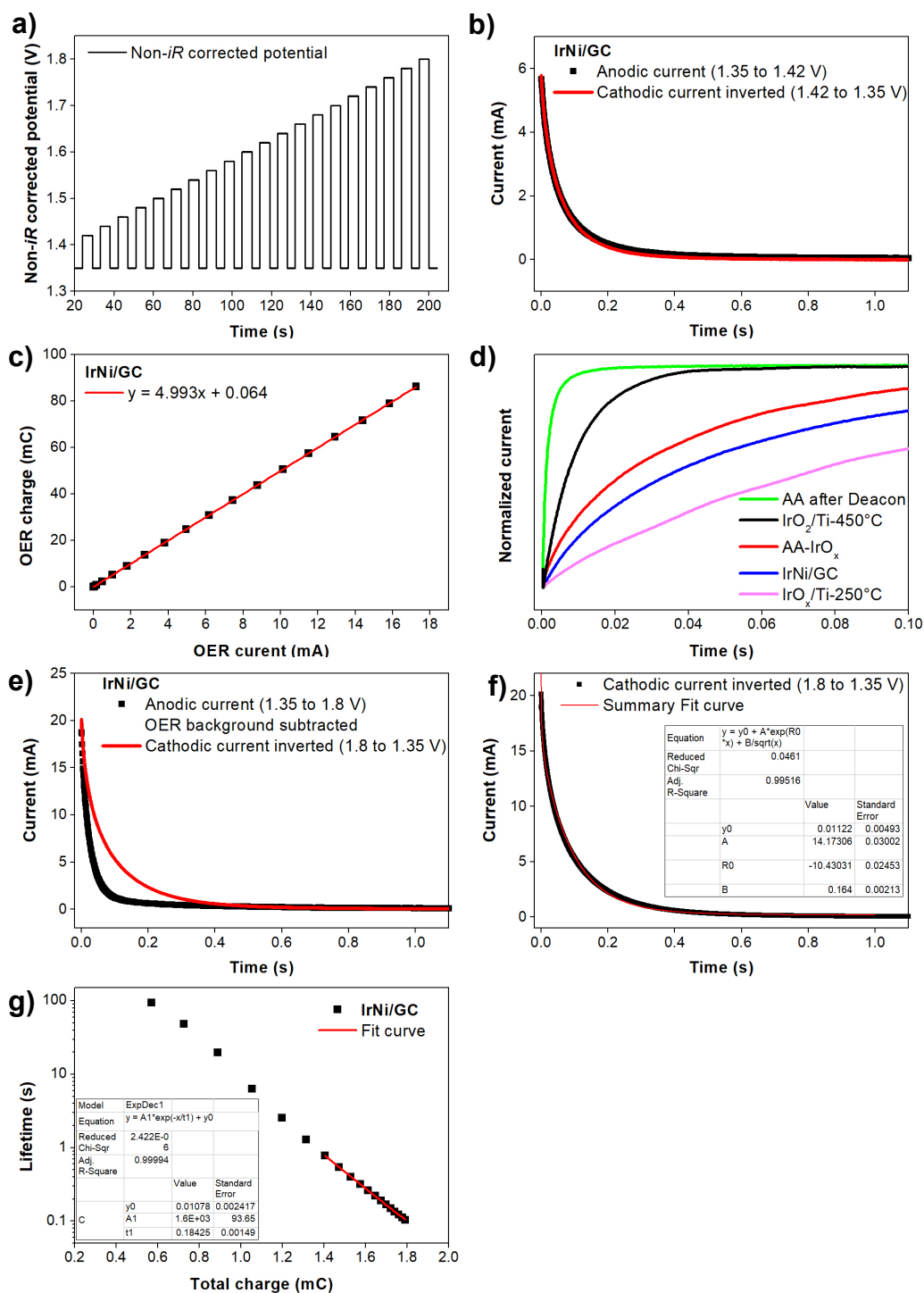
The charge integration scheme applied in the main text was developed to deal with the complication that the anodic current is a convolution of capacitive charge, catalyst oxidation and OER currents. To do so we note the cathodic current pulse can be related to the number of electrons injected into the oxidized catalyst to reduce it back to its state before the OER. Below the OER onset, the cathodic charge equals the anodic charge (Supplementary Fig. 1b, also see Supplementary Table 4 in the supplementary tables section), and the line shape of the current decay is essentially identical for both oxidation and reduction. We assume that charge conservation also holds once the OER sets in; thus, the integrals of the cathodic current pulses can be used to probe the amount of oxidative charge that was stored in the electrocatalyst at the applied anodic potential. That is, the anodic catalyst charge equals the inverse cathodic charge and the difference of the anodic and cathodic charge is the OER charge. The perfect correlation of OER current and thus derived OER charge, with a slope of 5 (i.e. 5 s time on OER in the anodic voltage steps) demonstrates the validity of our assumption of charge conservation (Supplementary Fig. 1c).

### Analysis of transient current response to voltage pulses

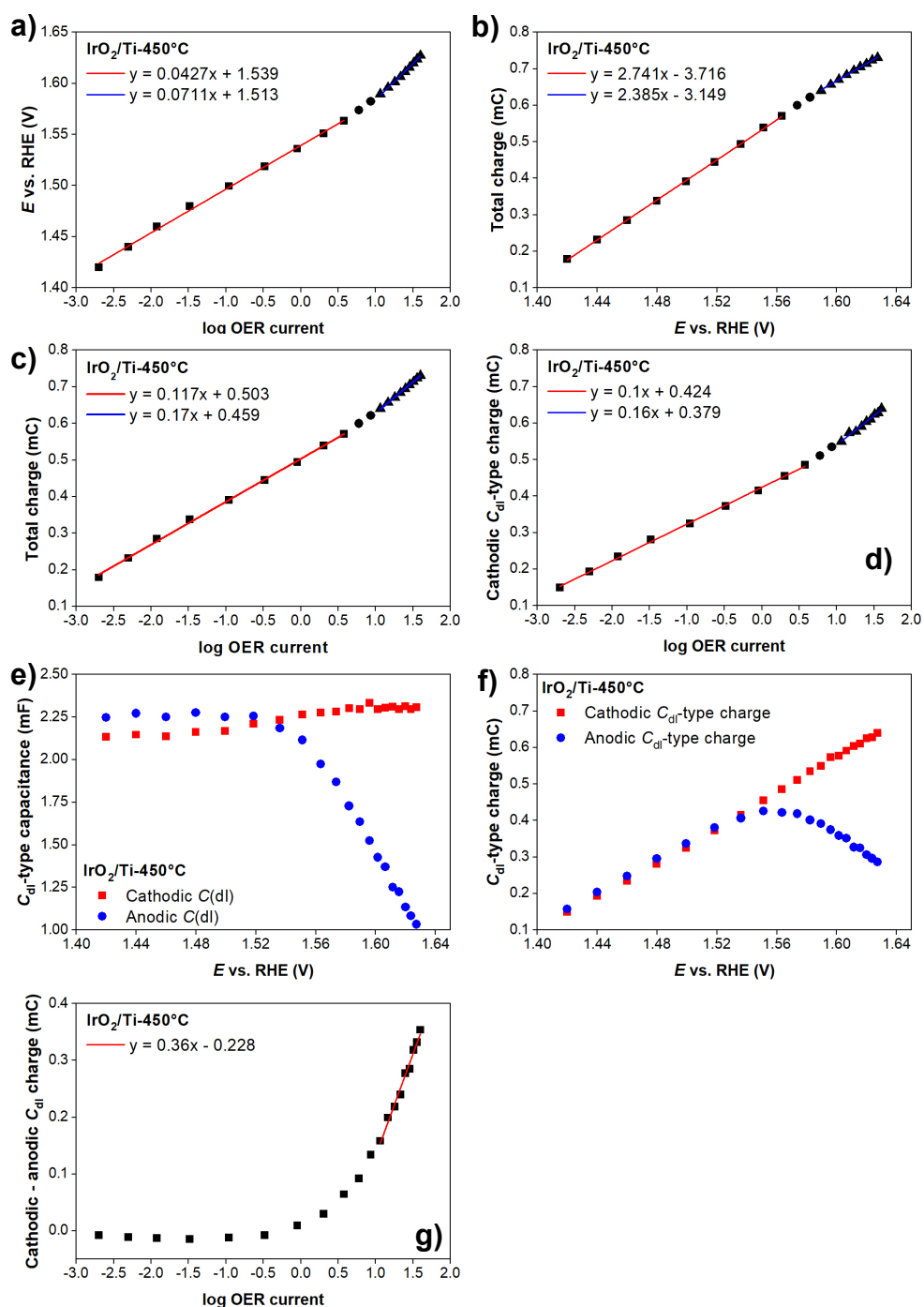
In addition to the steady-state data shown in the main text (Fig. 1), we analyzed the transient current response to the voltage steps using the Dupont and Donne model<sup>23</sup>, see Supplementary Figs. 1-9. As described below, this approach offers a largely semantic distinction between what is termed double layer ( $C_{dl}$ ) and diffusion limited pseudocapacitance ( $C_{diff}$ ). Some caution is, however, needed with this distinction. It arises from the shape of the temporal decay profile.  $C_{dl}$  is defined to account for the exponential current decay, while  $C_{diff}$  accounts for the slow power-law decay portion of the current profile. We stress that such a distinction is largely semantic, but we retain it to make connections with existing literature more transparent and use  $C_{dl}$ -type and  $C_{diff}$ -type to distinguish temporal profiles.

We find the catalyst's total pseudocapacitance is one to two orders of magnitude larger than the double layer capacitance of conductive planar electrodes. The time-dependence of the charging/discharging current of the Ir oxide materials upon voltage steps is, however, still of  $C_{dl}$ -type. The cathodic  $C_{dl}$ -type pseudocapacitive charge (pseudocapacitance times potential step) extracted from the

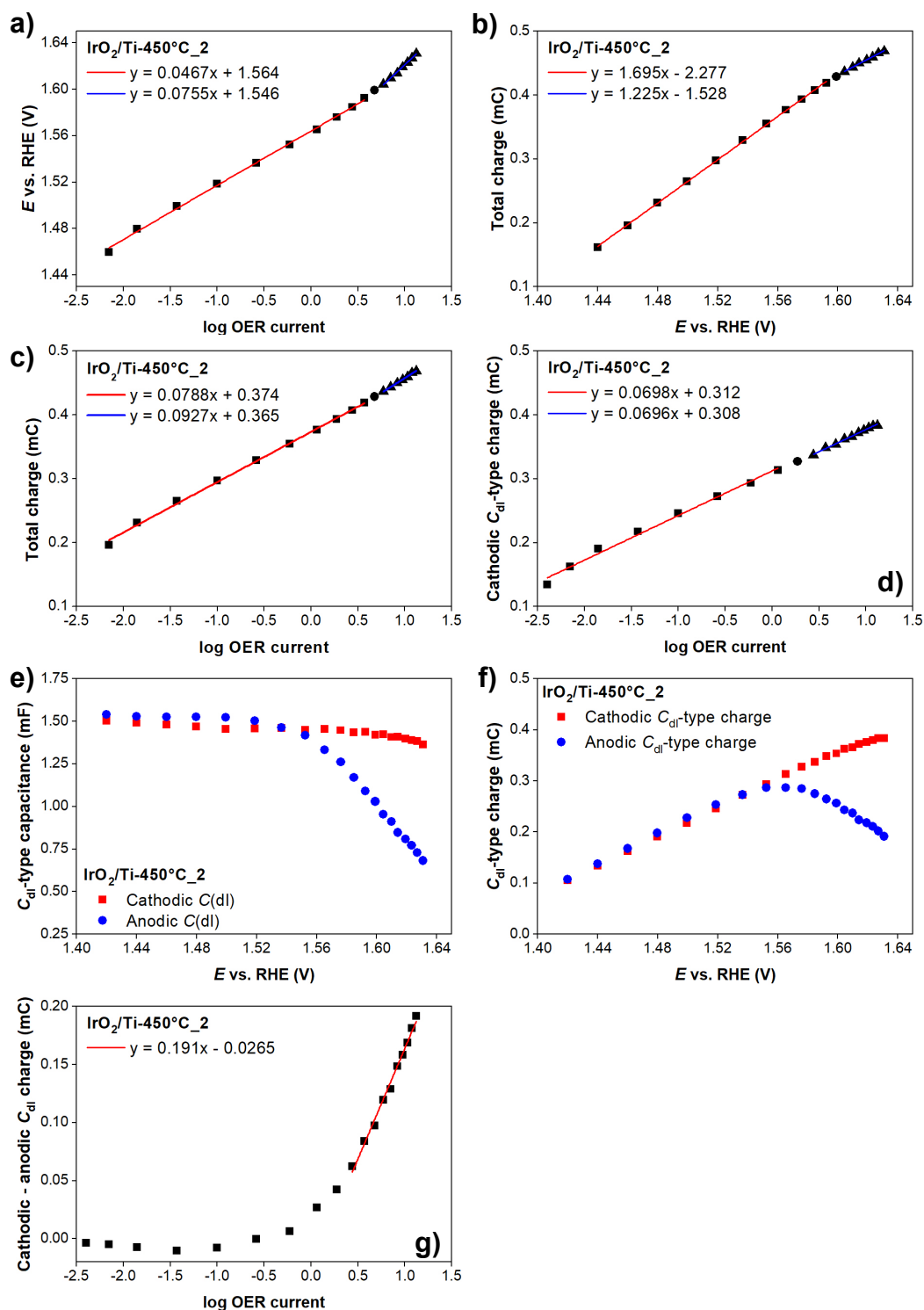
fit (Supplementary Fig. 8f) follows the total charge profiles as a function of potential (Supplementary Fig. 8b). At potentials where significant OER rates are observed, the capacitance values for the anodic current profiles are lower than the capacitance from the cathodic potential steps. As probed in the potential-step transients, the difference of the cathodic and anodic pseudocapacitive charge of  $C_{dl}$ -type as a function of the log OER current again shows a linear dependence (Supplementary Fig. 8g) when the lifetime of the charge is small and the OER rate is high. Further details of this analysis are given below.



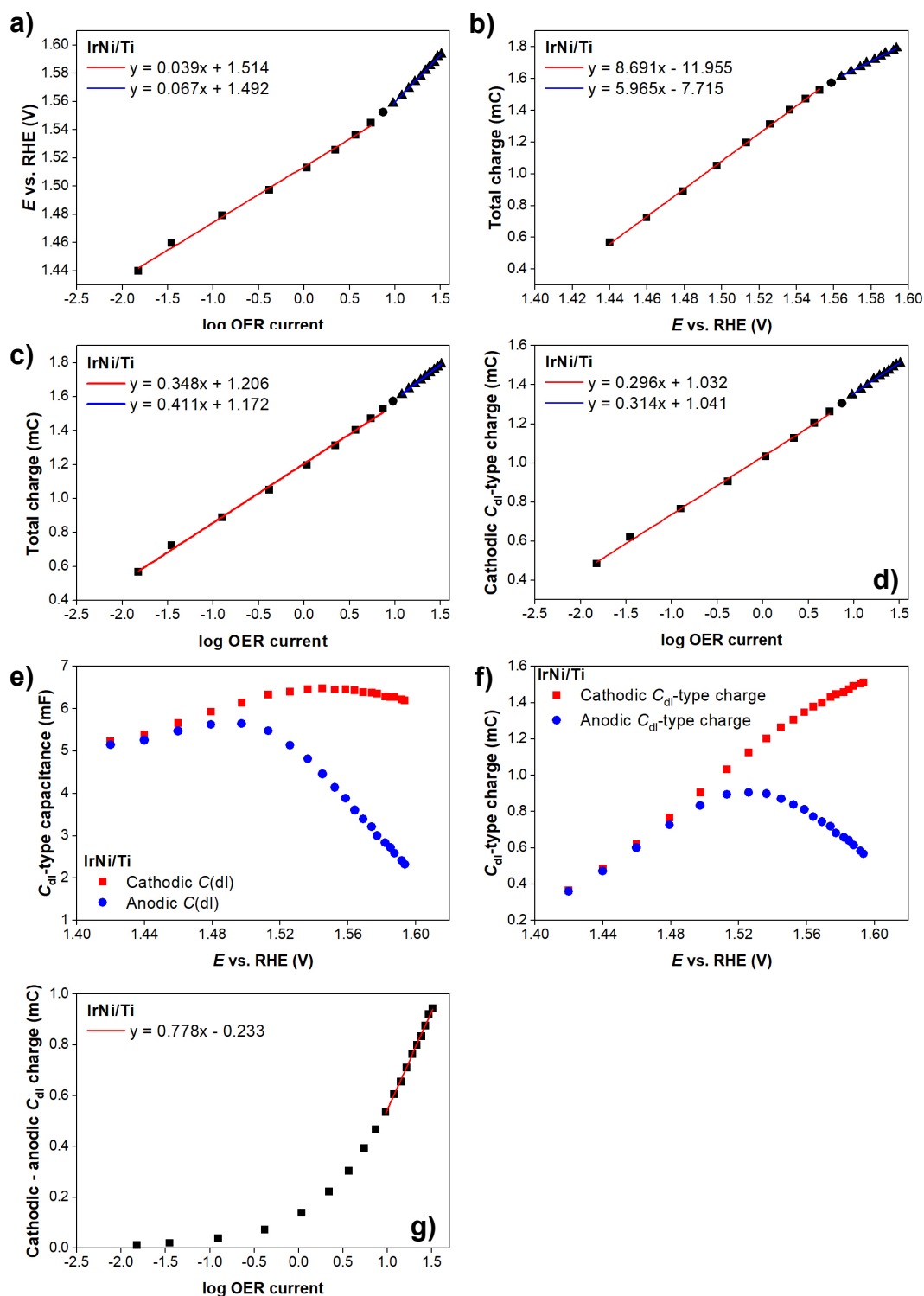
**Supplementary Fig. 1 | Pulse voltammetry protocol and response.** **a**, Pulse voltammetry protocol between 1.35 V cathodic and 1.42 V to 1.8 V anodic non-*i*R corrected potentials. **b**, First anodic and inverted cathodic current decay (IrNi/GC). **c**, OER charge (total anodic charge integral – total cathodic charge integral) vs. OER current. The slope is 5 because the anodic pulse was 5 s. **d**, Normalized current response to potential step (1.42 V to 1.35 V) for selected samples. **e**, Comparison of anodic current decay after background subtraction (step from 1.35 V to 1.8 V) with the inverted cathodic current signal upon the reverse (1.8 V to 1.35 V). **f**, Example of fitting transient current decay with the 3-component fit model (see below). **g**, The lifetime of the charge (defined by dividing the total charge with the OER current) as a function of the total charge.



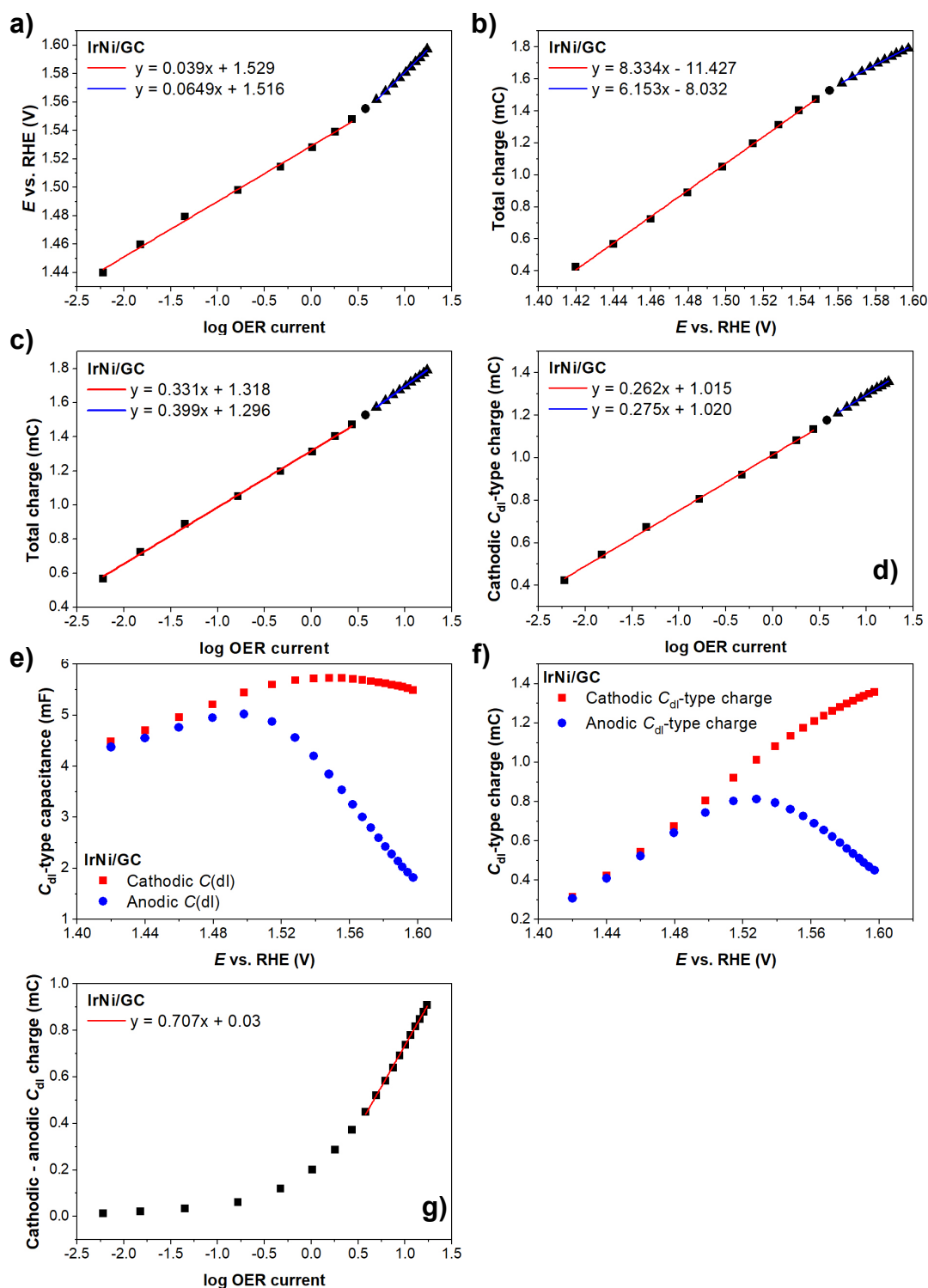
**Supplementary Fig. 2 | Measured electrocatalytic response of  $\text{IrO}_x/\text{Ti-450}^\circ\text{C}$ .** **a**,  $iR$  corrected potential vs. log OER current, Tafel plot, from pulse voltammetry. **b**, Total charge (integral cathodic charge) vs.  $iR$  corrected potential from pulse voltammetry. **c**, Total charge (integral cathodic charge) vs. log OER current from pulse voltammetry. **d**, Cathodic  $C_{dl}$ -type charge vs. log OER current. **e**,  $C_{dl}$ -type capacitance derived from fitting the current profiles of the pulse voltammetry measurement. Cathodic (Anodic): fit of the cathodic (anodic) current profiles upon the potential steps from anodic (cathodic) to cathodic (anodic). **f**,  $C_{dl}$ -type charge vs. the  $iR$  corrected potential. **g**, The difference between cathodic and anodic  $C_{dl}$ -type charge (from **f**) vs. log OER current. Sample: fresh  $\text{IrO}_2/\text{Ti-450}^\circ\text{C}$ . OER current in **a**, **c**, **d**, and **g** is in mA.



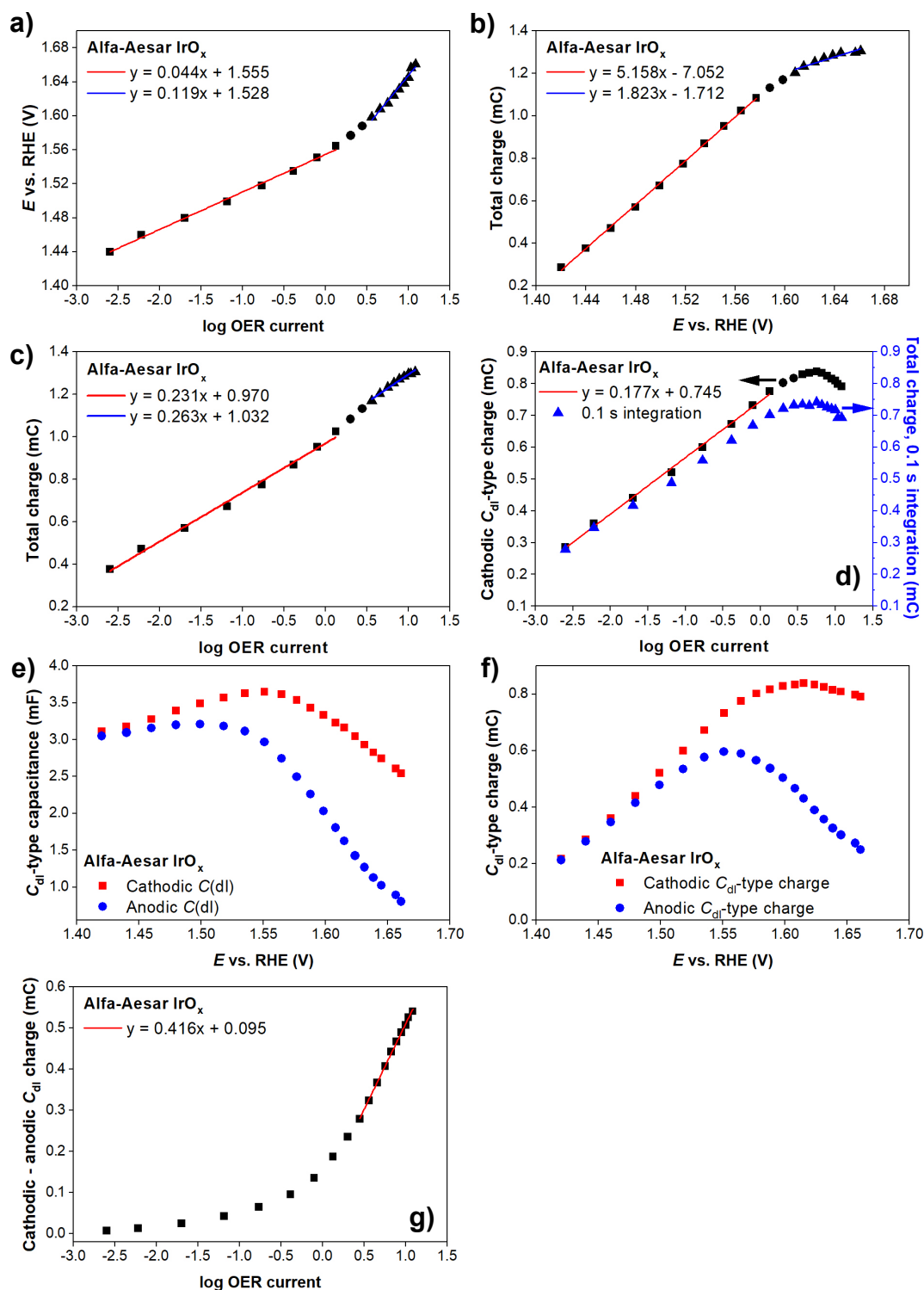
**Supplementary Fig. 3 | Measured electrocatalytic response of used  $\text{IrO}_x/\text{Ti-450}^\circ\text{C}$ .** **a**,  $iR$  corrected potential vs. log OER current, Tafel plot, from pulse voltammetry. **b**, Total charge (integral cathodic charge) vs.  $iR$  corrected potential from pulse voltammetry. **c**, Total charge (integral cathodic charge) vs. log OER current from pulse voltammetry. **d**, Cathodic  $C_{dl}$ -type charge vs. log OER current. **e**,  $C_{dl}$ -type capacitance derived from fitting the current profiles of the pulse voltammetry measurement. **f**,  $C_{dl}$ -type charge vs. the  $iR$  corrected potential. **g**, The difference between cathodic and anodic  $C_{dl}$ -type charge (from **f**) vs. log OER current. Sample: partially deactivated  $\text{IrO}_2/\text{Ti-450}^\circ\text{C}$ . OER current in **a**, **c**, **d**, and **g** is in mA.



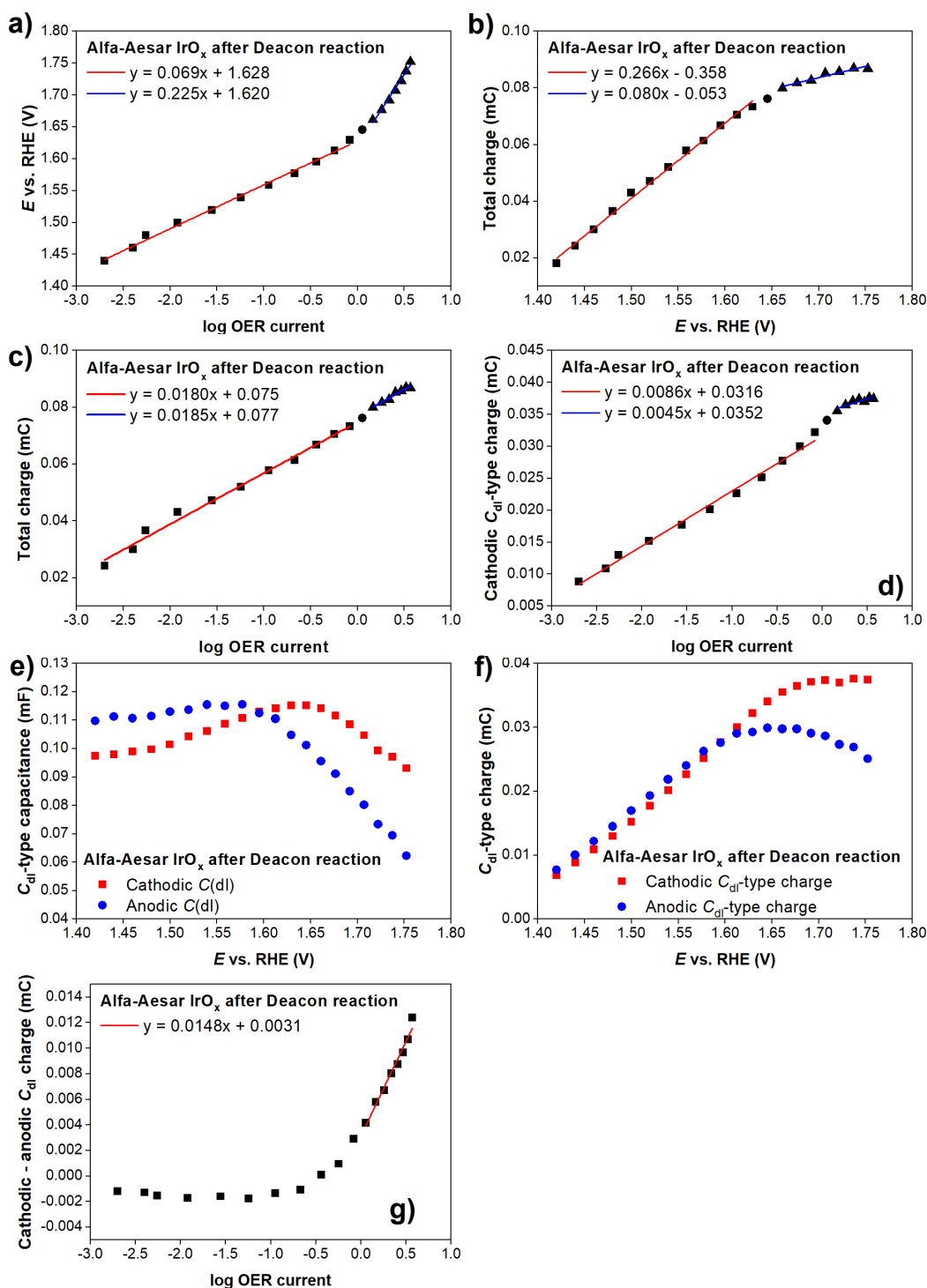
**Supplementary Fig. 4 | Measured electrocatalytic response of IrNi/Ti.** **a**,  $iR$  corrected potential vs. log OER current, Tafel plot, from pulse voltammetry. **b**, Total charge (integral cathodic charge) vs.  $iR$  corrected potential from pulse voltammetry. **c**, Total charge (integral cathodic charge) vs. log OER current from pulse voltammetry. **d**, Cathodic  $C_{dl}$ -type charge vs. log OER current. **e**,  $C_{dl}$ -type capacitance derived from fitting the current profiles of the pulse voltammetry measurement. **f**,  $C_{dl}$ -type charge vs. the  $iR$  corrected potential. **g**, The difference between cathodic and anodic  $C_{dl}$ -type charge (from **f**) vs. log OER current. Sample: IrNi/Ti. OER current in **a**, **c**, **d**, and **g** is in mA.



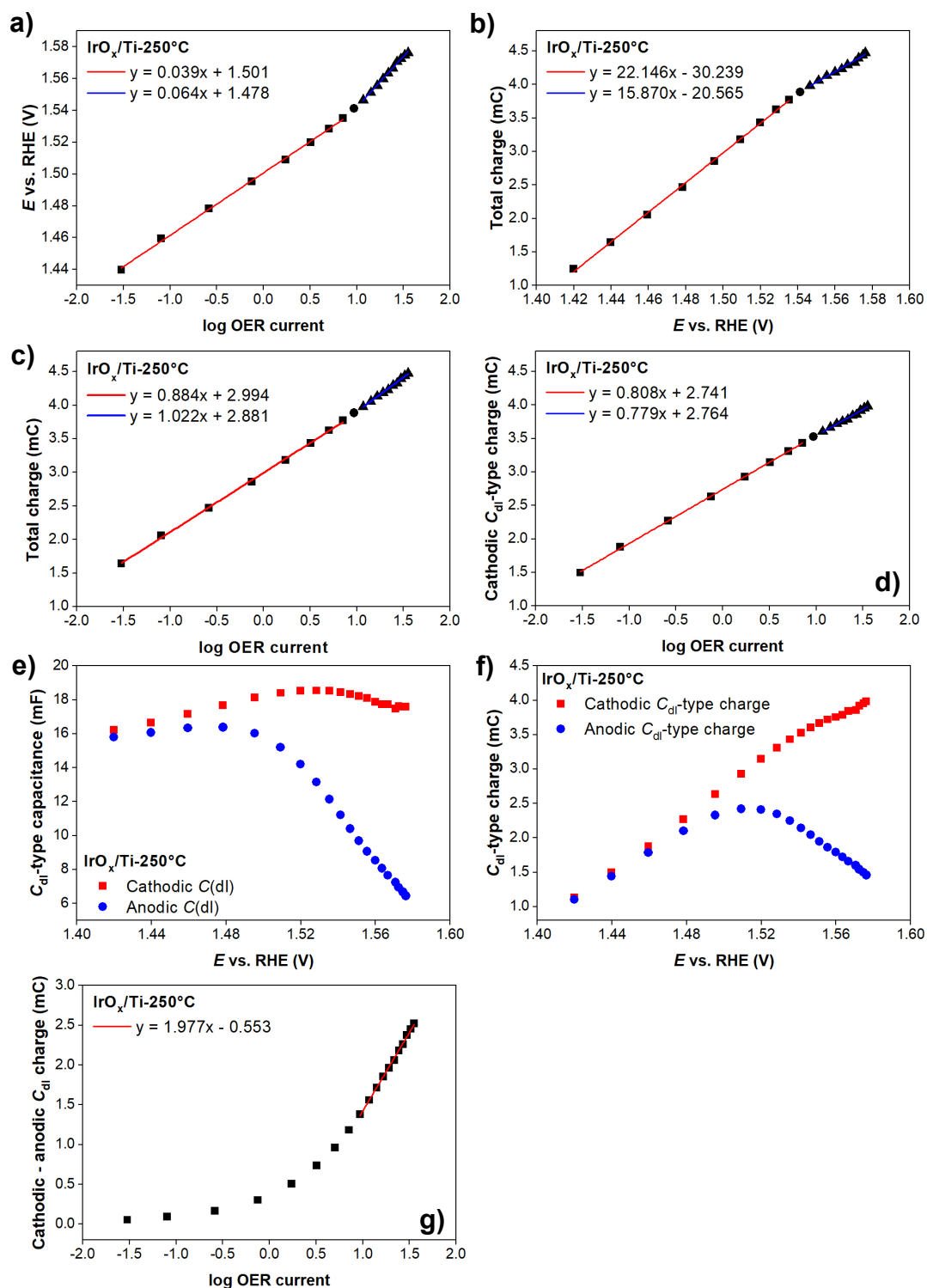
**Supplementary Fig. 5 | Measured electrocatalytic response of IrNi/GC.** **a**,  $iR$  corrected potential vs.  $\log$  OER current, Tafel plot, from pulse voltammetry. **b**, Total charge (integral cathodic charge) vs.  $iR$  corrected potential from pulse voltammetry. **c**, Total charge (integral cathodic charge) vs.  $\log$  OER current from pulse voltammetry. **d**, Cathodic  $C_{dl}$ -type charge vs.  $\log$  OER current. **e**,  $C_{dl}$ -type capacitance derived from fitting the current profiles of the pulse voltammetry measurement. **f**,  $C_{dl}$ -type charge vs. the  $iR$  corrected potential. **g**, The difference between cathodic and anodic  $C_{dl}$ -type charge (from **f**) vs.  $\log$  OER current. Sample: IrNi/GC (GC: glassy carbon). OER current in **a**, **c**, **d**, and **g** is in mA.



**Supplementary Fig. 6 | Measured electrocatalytic response of Alfa-Aesar IrO<sub>x</sub>.** **a**, *iR* corrected potential vs. log OER current, Tafel plot, from pulse voltammetry. **b**, Total charge (integral cathodic charge) vs. *iR* corrected potential from pulse voltammetry. **c**, Total charge (integral cathodic charge) vs. log OER current from pulse voltammetry. **d**, Cathodic C<sub>dl</sub>-type charge vs. log OER current. **e**, C<sub>dl</sub>-type capacitance derived from fitting the current profiles of the pulse voltammetry measurement. **f**, C<sub>dl</sub>-type charge vs. the *iR* corrected potential. **g**, The difference between cathodic and anodic C<sub>dl</sub>-type charge (from **f**) vs. log OER current. Sample: commercial Alfa-Aesar IrO<sub>x</sub> powder. OER current in **a**, **c**, **d**, and **g** is in mA.



**Supplementary Fig. 7 | Measured electrocatalytic response of Alfa-Aesar IrO<sub>x</sub> post-Deacon.** **a**,  $iR$  corrected potential vs.  $\log$  OER current, Tafel plot, from pulse voltammetry. **b**, Total charge (integral cathodic charge) vs.  $iR$  corrected potential from pulse voltammetry. **c**, Total charge (integral cathodic charge) vs.  $\log$  OER current from pulse voltammetry. **d**, Cathodic C<sub>dl</sub>-type charge vs.  $\log$  OER current. **e**, C<sub>dl</sub>-type capacitance derived from fitting the current profiles of the pulse voltammetry measurement. **f**, C<sub>dl</sub>-type charge vs. the  $iR$  corrected potential. **g**, The difference between cathodic and anodic C<sub>dl</sub>-type charge (from **f**) vs.  $\log$  OER current. Sample: commercial Alfa-Aesar IrO<sub>x</sub> powder after treatment in the Deacon reaction. OER current in **a**, **c**, **d**, and **g** is in mA.



**Supplementary Fig. 8 | Measured electrocatalytic response of IrO<sub>x</sub>/Ti-250°C.** **a**, *iR* corrected potential vs. log OER current, Tafel plot, from pulse voltammetry. **b**, Total charge (integral cathodic charge) vs. *iR* corrected potential from pulse voltammetry. **c**, Total charge (integral cathodic charge) vs. log OER current from pulse voltammetry. **d**, Cathodic C<sub>dl</sub>-type charge vs. log OER current. **e**, C<sub>dl</sub>-type capacitance derived from fitting the current profiles of the pulse voltammetry measurement. **f**, C<sub>dl</sub>-type charge vs. the *iR* corrected potential. **g**, The difference between cathodic and anodic C<sub>dl</sub>-type charge (from **f**) vs. log OER current. Sample: IrO<sub>x</sub>/Ti-250°C. OER current in **a**, **c**, **d**, and **g** is in mA.

Dupont and Donne<sup>23</sup> analyzed the (pseudo)capacitive behavior of common electrochemical capacitors using step potential electrochemical spectroscopy, which is similar to the pulse voltammetry technique applied here. The decaying current profile can be fit to known theoretical current-time profiles related to different types of charge storage mechanism. The current profile for a double layer capacitor in series with a resistor upon the application of a potential step can be described by:

$$i_{\text{dl}} = \frac{E}{R_s} \exp\left(-\frac{t}{R_s C_{\text{dl}}}\right) \quad (\text{Supplementary Eq. 10})$$

where the  $R_s$  is the series resistance (in  $\Omega$ ) related to the resistance of the electrolyte, the electrode and the materials in the cell;  $C_{\text{dl}}$  is the double layer capacitance (F) of  $C_{\text{dl}}$ -type;  $t$  is the time (in s) after the potential ( $E$ , in V) step.

Double layer charging, however, may not be the only charge storage mechanism. Slower, diffusion limited processes can also occur. In their simplest form these processes are described by the Cottrell equation for semi-infinite planar diffusion<sup>24</sup>:

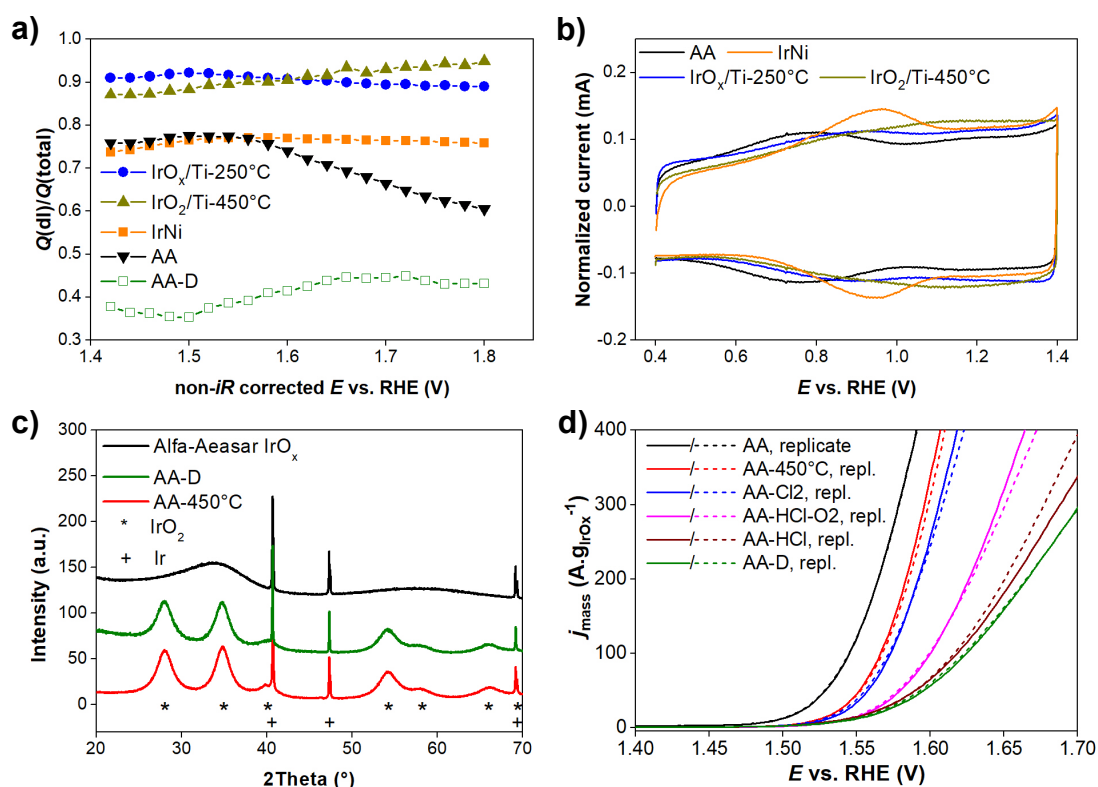
$$i_{\text{d}} = \frac{k}{\sqrt{t}} \quad (\text{Supplementary Eq. 11})$$

giving rise to  $C_{\text{diff}}$ -type diffusion limited pseudocapacitance, where  $k$  is constant. In general, pseudocapacitive redox charge storage is associated with such a diffusion limited process. However, we show that the main part of charge storage of the Ir materials is of  $C_{\text{dl}}$ -type.

To help demonstrate the above finding, Supplementary Fig. 1d shows the first 0.1 s of the intensity normalized temporal current profile of five Ir samples upon a cathodic voltage pulse from 1.42 V to 1.35 V. The time constant of the current response varies ca. two orders of magnitude; the current of the commercial Alfa-Aesar  $\text{IrO}_x$  sample after Deacon treatment ( $4\text{HCl} + \text{O}_2 \leftrightarrow 2\text{Cl}_2 + 2\text{H}_2\text{O}$ ) is roughly two orders of magnitude faster to decay than that of an amorphous  $\text{IrO}_x$  prepared by low-T (250 °C) calcination. Due to the faster exponential dependence of  $C_{\text{dl}}$ -type charge storage (vs. inverse square root dependence for  $C_{\text{diff}}$ -type), the difference in initial time dependences is dominated by differences in  $C_{\text{dl}}$ -type capacitance. Supplementary Tables 1 and 2 in the supplementary tables section compile the capacitance values of a number of samples based on different evaluation methods, including integration of the current profile (total capacitance), fit of the temporal

profile to extract  $C_{dl}$ -type capacitance, scan rate variation of cyclic voltammetry (total capacitance and outer capacitance) and impedance spectroscopy (double layer and pseudocapacitance). As the tabulated values indicate, every method finds the same ordering of the sample capacitance. Furthermore, though the capacitance values vary, there is reasonable agreement between the total capacitance values based on charge integration and scan rate variation. Outer and  $C_{dl}$ -type capacitance values are, as a rule, lower than total capacitance. It is clear that  $C_{dl}$ -type charging is the dominant contribution to the total charge. We note that the double layer capacitance of conducting planar electrodes is typically a few tens of  $\mu\text{F}/\text{cm}^2$ , one to two orders of magnitude lower than the capacitance values of the  $\text{IrO}_x$  samples with known BET surface areas observed in this work. Therefore, we probe pseudocapacitance.

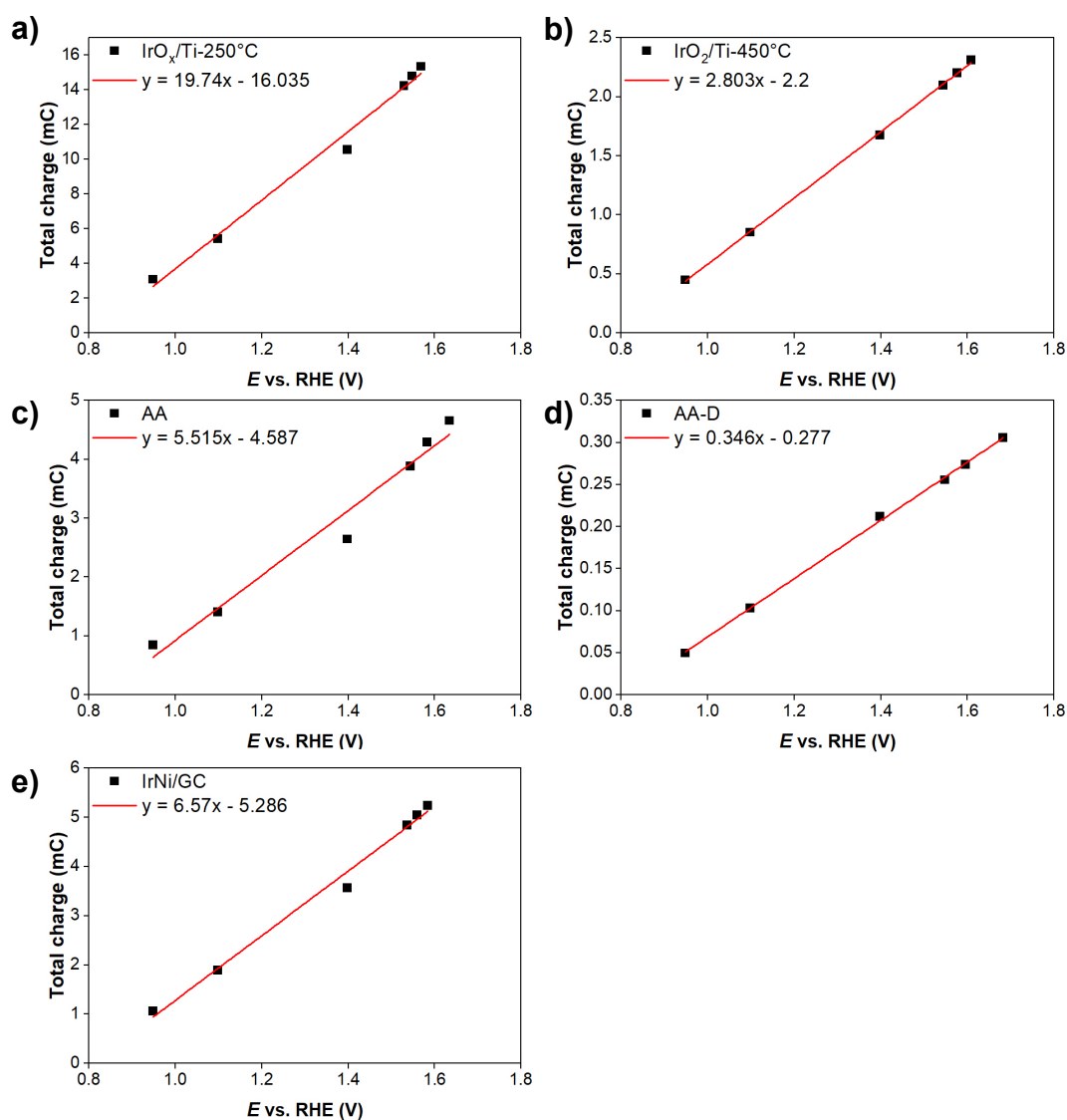
In our simple fit model we used the  $C_{dl}$ -type and  $C_{diff}$ -type types of current terms to describe the voltage steps; that is, Supplementary Eqs. 10 and 11 with an additional constant, time independent term, due to the fact that the current normally does not decay exactly to zero. Supplementary Fig. 1f depicts a fit example and shows the quality of the fit with the standard deviation, suggesting that the quality of the fit is good enough to extract trends as a function of potential. The series resistance in our electrochemical cell (evaluated by impedance spectroscopy at various potentials) is normally in the range of  $10\ \Omega$  to  $15\ \Omega$  ( $\pm 5\ \Omega$ ) which was reproduced by the fit reasonably well, within a few Ohms accuracy. Our focus is however on the evolution of the  $C_{dl}$ -type capacitance, which, for  $\text{IrO}_x/\text{Ti}$ -250°C, is shown in Supplementary Fig. 8e; the results of the other samples are compiled in Supplementary Fig. 2-7. The cathodic  $C_{dl}$ -type capacitance extracted from the cathodic current profiles is a weak function of the potential, changing between 16 mF and 19 mF up to  $\sim 1.53\ \text{V}$ , above which it is slowly decreasing to 17.2 mF. These numbers are a few (1 to 3) mF lower than the estimates for the total capacitance based on the linear fits in Supplementary Fig. 8b. When the capacitance values are multiplied by the voltage step size (or  $i_{dl}$  is integrated over time), we get the  $C_{dl}$ -type charge as plotted in Supplementary Fig. 8f. The profile of cathodic  $C_{dl}$ -type charge (based on fitting the decaying current profile) follows the integral total charge profile very well; the only difference is that the  $C_{dl}$ -type charge is  $\sim 90\%$  of the total charge. Since the  $C_{dl}$ -type contribution to the total charge is practically independent of the potential (Supplementary Fig. 9a), the  $C_{dl}$ -type charge also perfectly correlates with the log OER current (cf. Supplementary Fig. 8d).



**Supplementary Fig. 9 | Additional analyses of samples.** **a**, The ratio of  $C_{dl}$ -type charge (as determined from the current profile analysis) and the total charge (integral analysis) as a function of the non- $iR$  corrected potential. **b**, Cyclic voltammetry of selected sample between 0.4 V to 1.4 V vs. RHE with 100  $mV s^{-1}$  scan rate. **c**, XRD patterns of the commercial Alfa-Aesar IrO<sub>x</sub> and its derivatives after treatment in the Deacon reaction (AA-D) and calcination at 450 °C in air (AA-450°C). The XRD patterns of IrO<sub>2</sub> and Ir are marked with \* and +, respectively. **d**, OER activity comparison of Alfa-Aesar IrO<sub>x</sub> after various treatments. Samples: AA: pristine sample, AA-450 °C: sample after calcination at 450 °C, AA-Cl<sub>2</sub>: calcined sample after treatment in Cl<sub>2</sub> at RT. AA-HCl-O<sub>2</sub>: calcined sample treated in HCl at 270 °C followed by treatment in O<sub>2</sub> at 300 °C. AA-HCl: calcined sample treated in HCl at 270 °C, AA-D: pristine sample treated in the Deacon reaction.

A tempting explanation for the correlation of log OER current and total charge would be through the  $C_{dl}$ -type charge. To show that this is not the case, we consider the case of amorphous Alfa-Aesar IrO<sub>x</sub> sample (Supplementary Fig. 6). Here the  $C_{dl}$ -type charge bends down at high potentials because charge storage in the bulk of the nanoparticles in the form of bulk ( $C_{diff}$ -type) redox trigger apparent loss of the  $C_{dl}$ -type capacitance and thus deviation from the observed linear dependence of the log OER current and  $C_{dl}$ -type charge. Bulk redox necessarily involves O uptake and release, which is in line with the observed appearance of lattice O in product O<sub>2</sub> when amorphous IrO<sub>x</sub> are used as OER catalysts<sup>25</sup>.

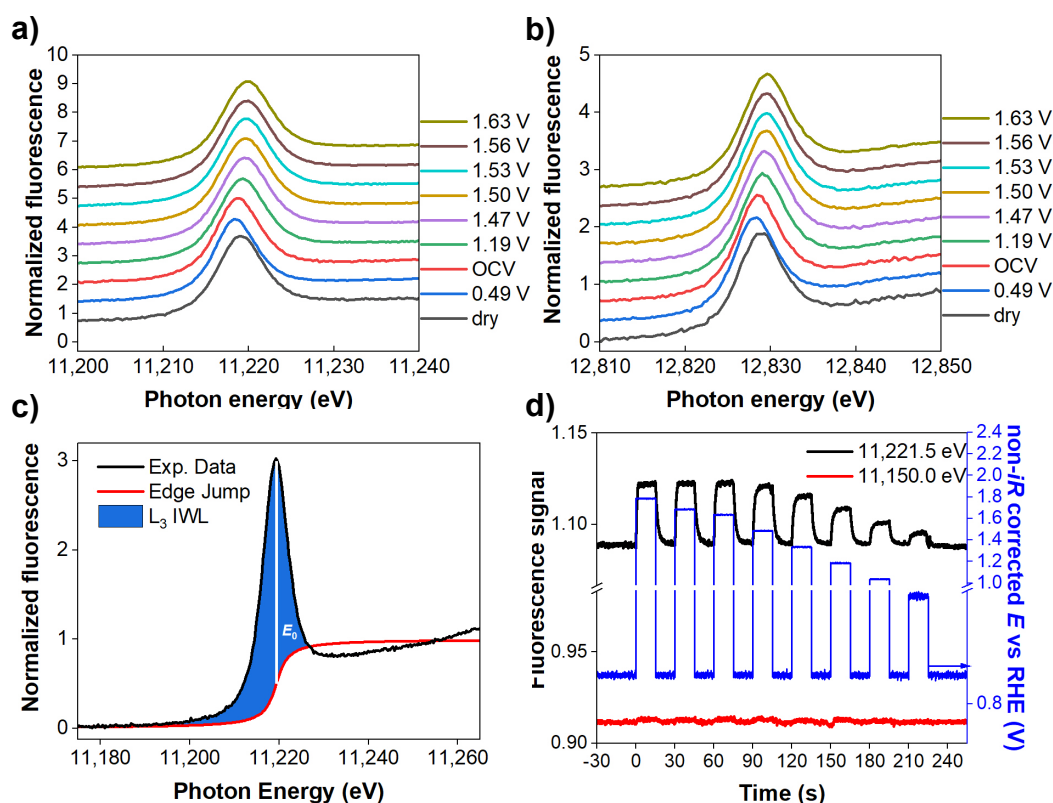
Although fitting the anodic current profiles results in higher uncertainties due to overlap with OER—and especially due to potentially changing OER rates over the course of the 5 s sampling time—we could nevertheless successfully extract  $C_{dl}$  from the anodic potential steps. The starting  $C_{dl}$ -type capacitance (as expected from Supplementary Fig. 1b) is very similar to that of  $C_{dl}$  for the cathodic potential steps, but at some intermediate potentials the two curves start to deviate. Above 1.51 V the anodic  $C_{dl}$  decreases rapidly with potential due to the much faster current decay in the anodic, as compared to the cathodic, voltage step when high anodic potentials are applied (Supplementary Fig. 1e). Consequently, the anodic  $C_{dl}$ -type charge (Supplementary Fig. 8f) drops significantly above 1.51 V. Although this observation may sound counterintuitive, the strong decrease of the anodic  $C_{dl}$  and anodic  $C_{dl}$ -type charge can be understood if we consider in detail what processes and states are probed in the anodic/cathodic voltage steps. In the cathodic step we probe the average resting state of the OER reaction going back to the “frozen”, unreactive state below OER. In the anodic step—when fast OER occurs, in the early part of the decay curve, which is sampled in  $C_{dl}$ —a synchronized source and sink is triggered: oxidation via the potential and reduction via some OER elementary steps and oxygen evolution itself. Thus, on average, a lower apparent capacitance should be observed. At low OER potentials, when the lifetime of the charge (formally defined by dividing the total charge by the OER current; Supplementary Fig. 1g) is high enough (much larger than the time constant of the decay curve), the effect will be very small. Therefore, the anodic and cathodic capacitance lines stay very close to each other, and here we probe probably only some early elementary steps of the reaction. Once, however, the reaction becomes fast—and the lifetime of the charge is low (on the order of the time constant of the current response)—the reduction of the capacitance will be large. The difference of the cathodic and anodic  $C_{dl}$ -type charge as probed in this synchronized short time transient as a function of the log OER current (Supplementary Fig. 8g) again shows a linear dependence once the lifetime of the charge is short and the OER rate is high. Thus, both the steady-state data (Fig. 1d) and transient results (Supplementary Fig. 8g) suggest that the log OER rate is a linear function of the oxidative charge accumulated on the catalyst. The total charge of selected samples determined in a broad potential window is shown in Supplementary Fig. 10.



**Supplementary Fig. 10 | Total charge of selected samples.** Charge determined by integral pulse voltammetry analysis in the broad potential window. Protocol: cathodic potential: 0.75 V, anodic potentials: 0.95 V to 1.7 V non- $iR$  corrected potentials. The figure plots the  $iR$  corrected potentials. Samples as marked.

#### Ir L-edge details

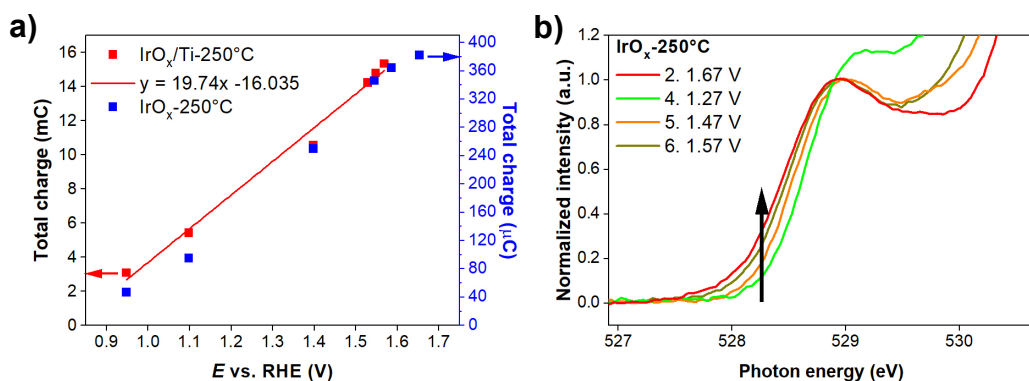
$L_3$  (Supplementary Fig. 11a) and  $L_2$  (Supplementary Fig. 11b) spectra were edge jump normalized. The white line (WL) areas were determined by numerical integration after subtracting an arctangent background centered at the WL maximum with unit height and 2 eV width<sup>26</sup>, see Supplementary Fig. 11c. Supplementary Fig. 11d shows the operando potentiodynamic XAS protocol using  $h\nu = 11,221.5$  eV (11,150.0 eV background signal below the Ir  $L_3$ -edge) during PV (0.84 V to 1.54 V with 15 s pulses, 1 ms spectral recording time). We verified FY equilibration to ensure charge transfer is not kinetically limited.



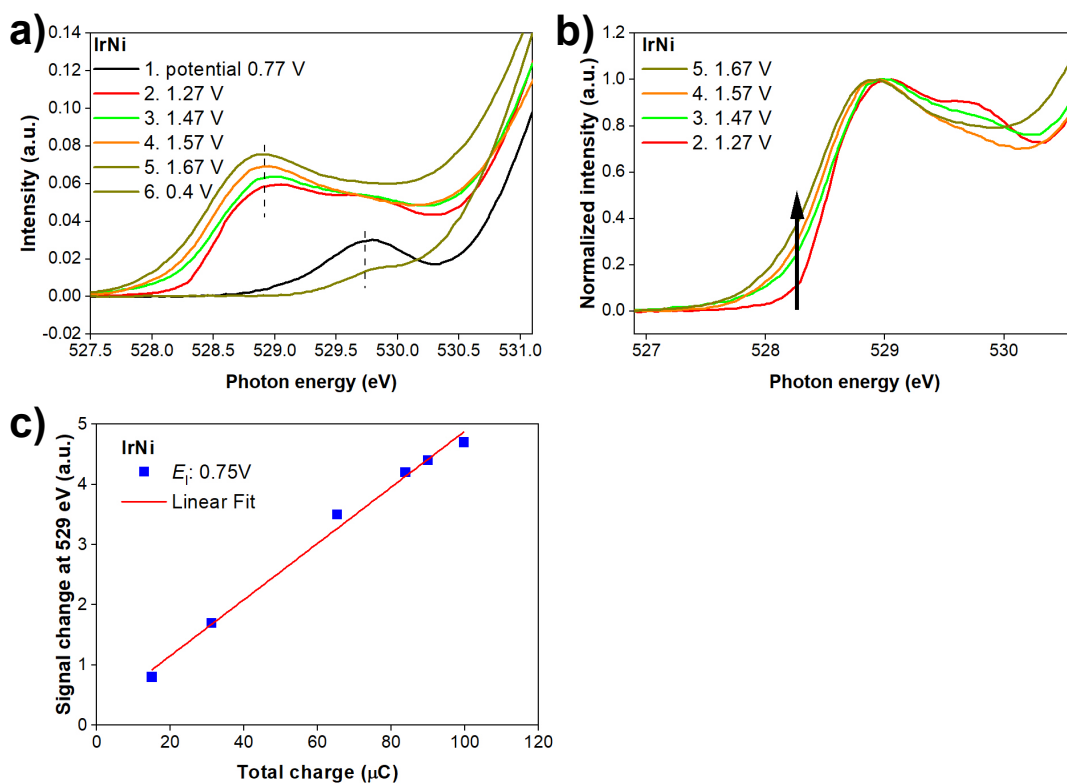
**Supplementary Fig. 11 | Ir L<sub>2,3</sub> white line analysis and pulsing protocol.** **a**, and **b**, Steady-state operando Ir L<sub>2,3</sub>-edge X-ray absorption spectra of IrO<sub>x</sub>/Ti-250°C at selected potentials at the L<sub>3</sub> and L<sub>2</sub> edge, respectively. **c**, The schematics of white line (WL) area determination applied to the Ir L-edge XAS spectra. The WL area (blue area) was determined assuming an arctan edge jump (unit height, width 2 eV) to model the continuum step positioned at the WL maximum following<sup>26</sup>. **d**, The protocol of operando potentiodynamic XAS experiment following the fluorescence signal evolution at two selected energies (11,221.5 eV at the Ir L<sub>3</sub> white line and 11,150.0 eV, below the Ir L<sub>3</sub> white line) The figure shows reversible positive signal evolution at the white line upon anodic polarization in line with catalyst's oxidation.

### O K-edge details

From Supplementary Fig. 12, the operando measurement on IrO<sub>x</sub>-250°C can be seen to recover the trends observed in a standard 3-compartment electrochemical cell, though the lower catalyst loading in the operando experiment results in a lower magnitude of stored charge. Supplementary Fig. 12 shows steady-state operando O K-edges of IrO<sub>x</sub>-250°C after scaling at 528.9 eV, where coloring indicates the applied bias. Similarly, operando steady-state and PV results are shown for IrNi Supplementary Fig. 13.



**Supplementary Fig. 12 | O K-edge XAS results for IrO<sub>x</sub>/Graphene-250 °C.** **a**, Total charge (integral cathodic charge) vs. *iR* corrected potential derived from pulse voltammetry using a potential window of 0.95 V to 1.70 V (non-*iR* corrected) with a resting potential at 0.75 V. Two low temperature (250 °C) calcined IrO<sub>x</sub> samples are overlaid: IrO<sub>x</sub>/Ti-250°C measured in a standard 3-compartment electrochemical cell and IrO<sub>x</sub>/Graphene-250°C in an operando O K-edge XAS experiment. Note the low magnitude of charge in the operando experiment is due to low catalyst loading. **b**, Steady-state operando O K-edge X-ray absorption spectra of IrO<sub>x</sub>/Graphene-250 °C at selected (non-*iR* corrected) potentials after scaling the spectra at 528.9 eV.



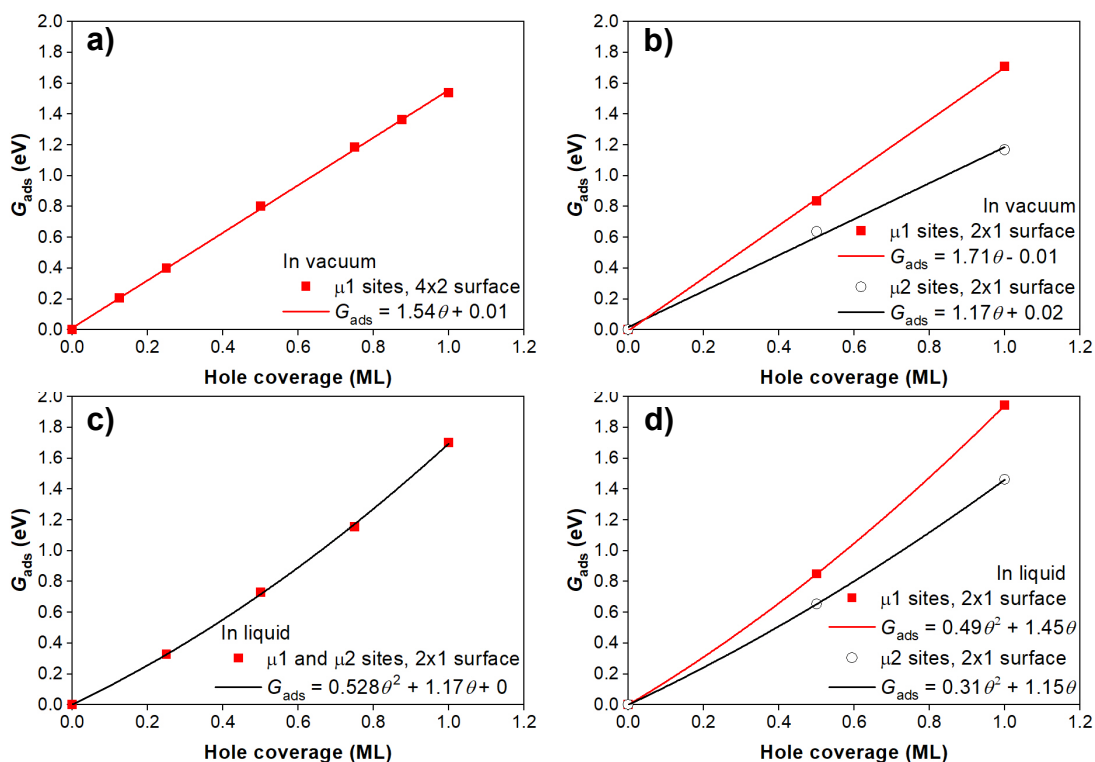
**Supplementary Fig. 13 | O K-edge XAS results for IrNi/Graphene.** **a**, Steady-state operando O K-edge X-ray absorption spectra of IrNi/Graphene at selected (non-*iR* corrected) potentials in the order indicated. **b**, Steady-state operando O K-edge spectra of IrNi/Graphene at selected (non-*iR* corrected) potentials after scaling the spectra at 528.9 eV. **c**, Correlation of the signal change of the O K-edge at 529 eV vs. the total charge derived from the pulse voltammetry using a potential window of 0.95 V to 1.70 V vs. RHE (non-*iR* corrected) with a resting cathodic potential at 0.75 V vs. RHE. Note the low magnitude of charge is due to low catalyst loading.

### **$E_a$ for $\mu_1$ -OH deprotonation**

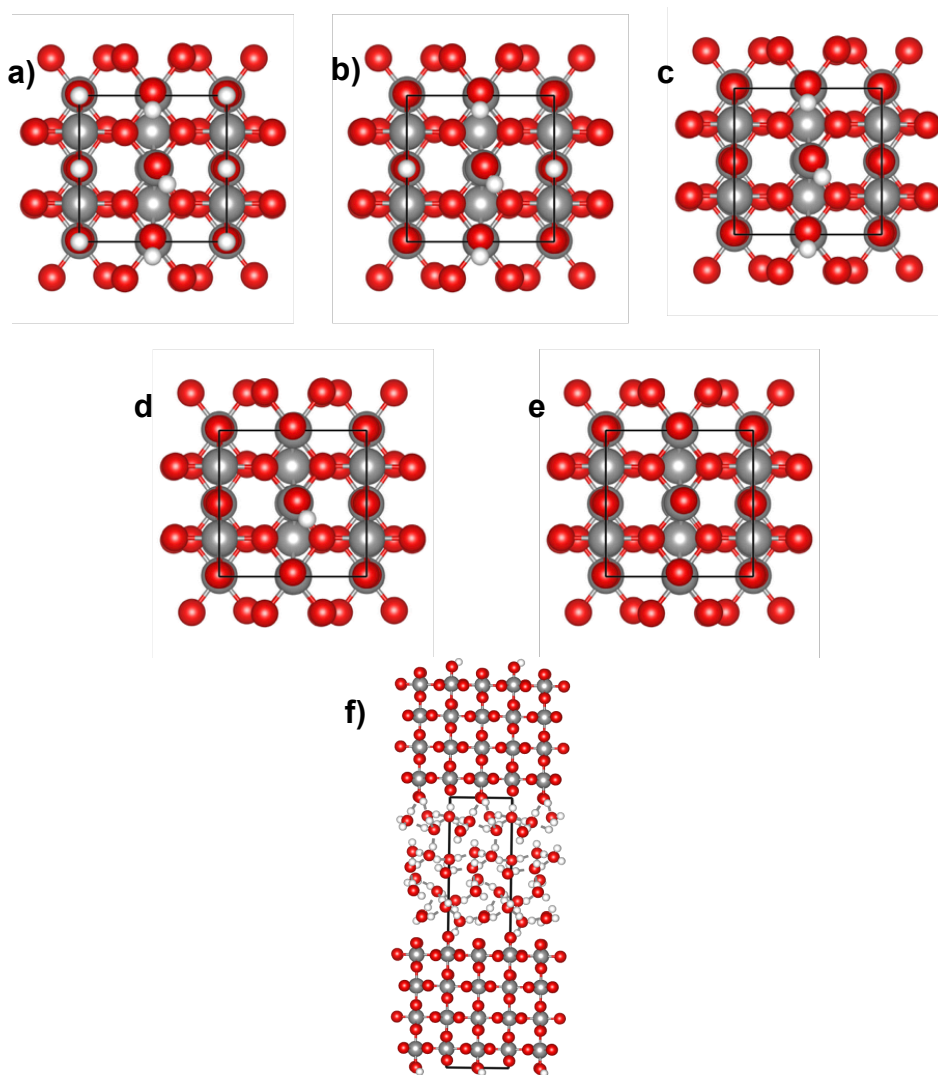
On the  $\mu_2$ -O/ $\mu_2$ -O and  $\mu_1$ -O/ $\mu_1$ -OH surface the activation energy for  $\mu_1$ -OH deprotonation with a constant charge is ca. 0.4 eV compared to the 0.67 eV for O-O coupling. Using a constant bias at the pzc leads to a reduction in both barriers to 0.30 eV and 0.63 eV, respectively. Thus, O-O formation appears to have higher activation energy than oxyl formation, and only O-O coupling is considered in the main text.

### **Frumkin behavior**

The interactions between adsorbed hydrogen were explored in vacuum using both a (2×4) and (1×2) cell in an effort to test if Frumkin dehydrogenation behavior is induced by the solvent or adatom interactions. Supplementary Fig. 14 demonstrates there is no appreciable interaction between the hydrogen atoms adsorbed on different sites (see Supplementary Fig. 15 for sites) in vacuum, as the adsorption free energy per  $H_{ads}$  is independent of coverage—determined by ab initio atomistic thermodynamics using an  $H_2$  reservoir at 1 bar and 298.15 K and including zero point energy. This implies Langmuir desorption behavior would be found in the absence of solvent. The quadratic behavior of the free energy associated with solvated H adsorption on the same sites (Supplementary Fig. 15) seen in Supplementary Fig. 14 demonstrates Frumkin behavior is present for the solvated surface. Thus, the chemical potential of adsorbed hydrogen,  $\mu_{ads} = \partial G / \partial \theta_{h^+}$  is described by  $\mu_{ads} = \mu_{ads}^0 + \gamma \theta_{h^+}$ , see Ref. <sup>27</sup>, with a Frumkin parameter ( $\gamma$ ) near unity for  $\mu_1$ -O (Supplementary Fig. 14d). This Frumkin behavior is manifest in the computed  $E$  vs. pH phase diagram, Fig. 3, which was computed using the data presented in Supplementary Fig. 14d as a single dataset. The computed phase diagram is in agreement with our experimental observations.



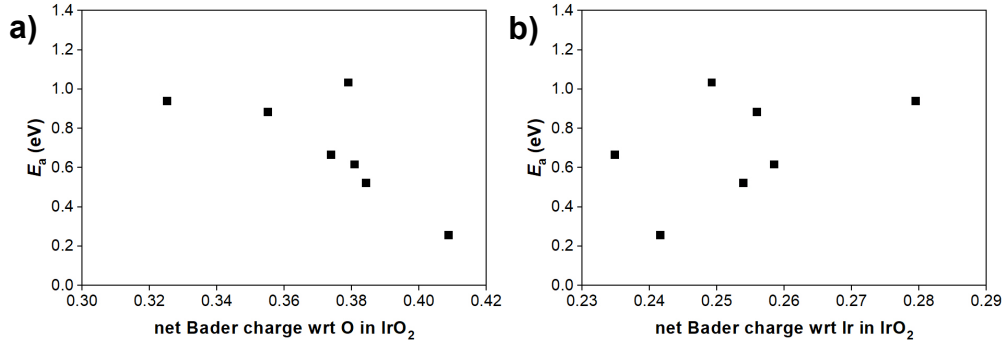
**Supplementary Fig. 14 | Adsorption free energy computed for H on O terminated IrO<sub>2</sub> (110).** Plotted as a function of the hole coverage (note the energy is normalized by the number of H adsorption sites to make the data on different surfaces more easily comparable). **a**,  $\mu_1$ -O sites for a (4x2) cell in vacuum. **b**,  $\mu_1$ -O and  $\mu_2$ -O sites for a (2x1) cell in vacuum. **c**, Total sites for a (2x1) cell in liquid. **d**, Separated  $\mu_1$ -O and  $\mu_2$ -O sites for a (2x1) cell in liquid.



**Supplementary Fig. 15 | Terminations of the (110) surface of IrO<sub>2</sub>.** **a**,  $\mu_2$ -OH/ $\mu_2$ -OH and  $\mu_1$ -OH/ $\mu_1$ -OH; **b**,  $\mu_2$ -O/ $\mu_2$ -OH and  $\mu_1$ -OH/ $\mu_1$ -OH; **c**,  $\mu_2$ -O/ $\mu_2$ -O and  $\mu_1$ -OH/ $\mu_1$ -OH; **d**,  $\mu_2$ -O/ $\mu_2$ -O and  $\mu_1$ -O/ $\mu_1$ -OH; **e**,  $\mu_2$ -O/ $\mu_2$ -O and  $\mu_1$ -O/ $\mu_1$ -O. **f**, Example of cell used to compute surface phase diagram. Ir atoms are grey, O as red, and H as white.

#### **$E_a$ for $\mu_1$ -OO coupling**

The reaction of H<sub>2</sub>O with  $\mu_1$ -O species on various surfaces, including with co-adsorbed O, OH, and Cl, was considered using the surfaces listed in Supplementary Table 7 in the supplementary tables section. The computed activation energies and the heats of reaction were used to generate the Brønsted–Evans–Polanyi relationship in the main text. Analysis of Bader charges of the  $\mu_1$ -O species (Supplementary Fig. 16), as well as the Ir it is bound to, suggests a drop in electron density on the  $\mu_1$ -O species associated with increased surface oxidation may contribute to the reduction in  $E_a$  found upon surface oxidation, independent of the chemical nature of the ligands introducing oxidative charge.



**Supplementary Fig. 16 | Bader charge and  $E_a$  for O-O coupling.** **a**, The activation energy for O-O coupling computed under the constant charge condition plotted against the Bader charge on the  $\mu_1$ -O involved in the reaction. **b**, The same energy plotted against the Bader charge on the Ir bound to the active  $\mu_1$ -O.

### Predicted OER current

At a sufficiently high overpotential the OER current can be described by its forward rate alone. As shown in the main text, this rate can be described by a Tafel-like equation by noting the rate constant for the electrode depends on the amount of charge stored in the material. In the case of a crystalline material like those investigated computationally, this is simply a dependence on surface coverage of oxidative charge (or hydrogen in the cases considered). The resulting Eq. 1 in the main text describes the general situation where a linear energy relationship mediates chemical bond making/breaking, reproduced here for convenience:

$$i = k_0 \theta_{\mu_1} \exp\left(-\frac{\zeta \theta_{h^+} + \kappa}{k_B T}\right) \quad (\text{Supplementary Eq. 12})$$

where the prefactor,  $k_0$ , is given by:

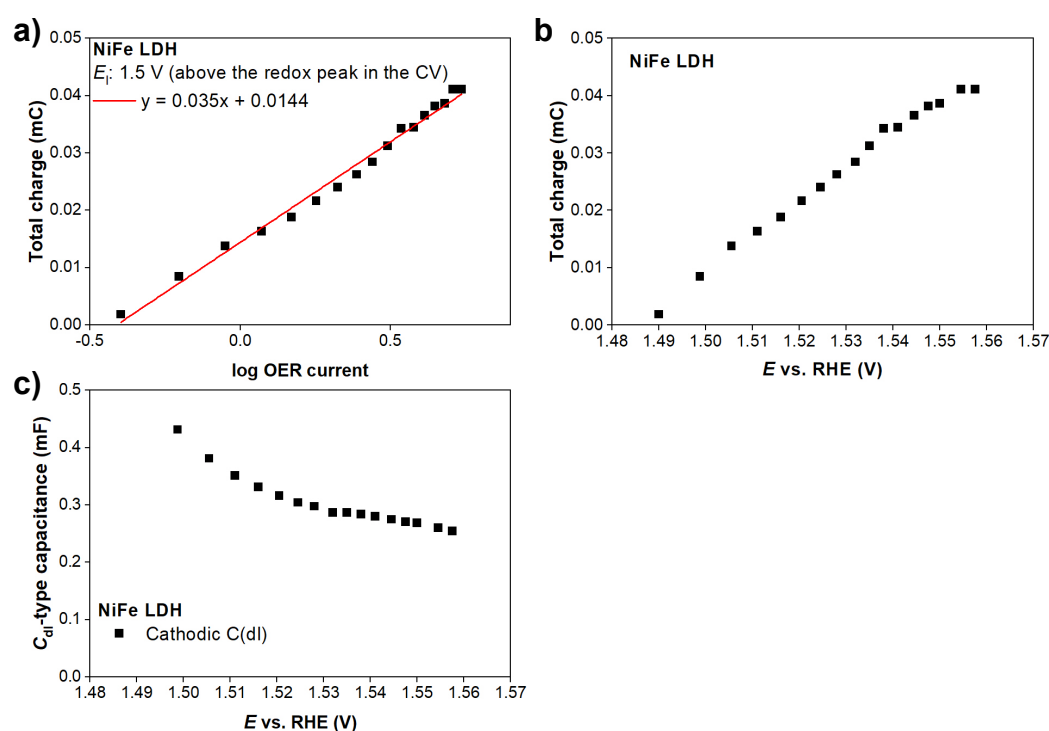
$$k_0 = 4 |e| \frac{k_B T}{h} N_{\mu_1} \quad (\text{Supplementary Eq. 13})$$

gives current in A. The factor of 4 in Supplementary Eq. 13 accounts for the 4 electrons transferred, and the constants take on their usual meaning:  $e$  is elementary charge,  $k_B$  Boltzmann's constant, and  $h$  Planck's constant.  $N_{\mu_1}$  is the number of sites, which was estimated using the BET area of AA-450°C (Supplementary Table 3 in the supplementary tables section) and the experimental catalyst loading (10  $\mu\text{g}_{\text{IrO}_x}$ ). For the results in Fig. 5 this assumption plays no role in the shape of the log current vs. potential (or log current vs.  $\theta_{h^+}$ ) profile, as  $k_0$  simply sets the magnitude of OER current. However, when describing temperature variations  $\Delta S^\ddagger$  may need to be explicitly included in  $k_0$ <sup>28</sup>. For our purposes Fig. 5 was created at 298.15 K using the hole coverage dependence on potential taken from the computed phase diagram (Fig.

3). In Fig. 5 the OER current was plotted in mA to facilitate comparison with experiment. The parameters  $\zeta$  and  $\kappa$  were taken from a fit of  $E_a$  to the O(H) covered (110) surfaces in Fig. 4c, excluding the activation energy with Cl, as we compare to a Cl free sample. The resulting equation,  $E_a = 1.23 \theta_{h^+} + 1.53$  (in eV), was used as a single data set in Supplementary Eq. 12 to generate the Tafel plot,  $\theta_{h^+}$  vs. potential, and  $\theta_{h^+}$  vs. log current plots shown in Fig. 5.

### NiFe LDH

PV measurements on Ni LDH followed the previously described protocol, though in 0.1M KOH with  $E_1 = 1.5$  V. The results are presented in Supplementary Fig. 17.

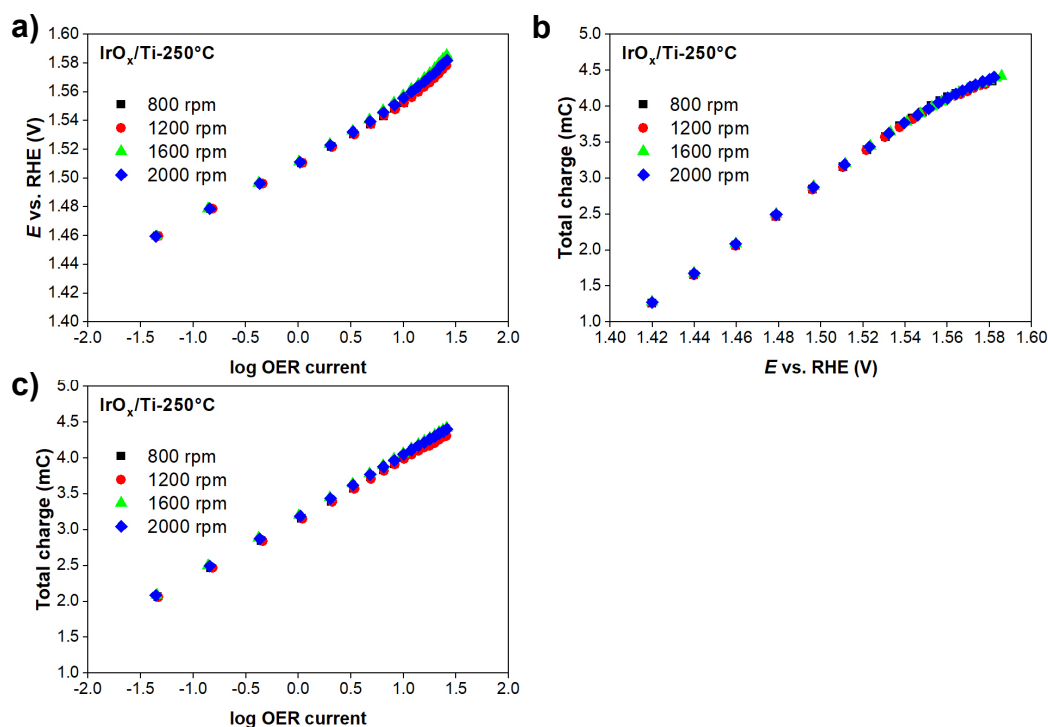


**Supplementary Fig. 17 | Electrochemical response of NiFe LDH.** **a**, Total charge (integral cathodic charge) vs. log OER current (mA) derived from the pulse voltammetry measurement. Sample: NiFe layered double hydroxide. The CV of the NiFe LDH contains a redox transition at the OER onset, and thus the constant cathodic potential was set to 1.5 V, above the redox transition. **b**, Total charge (integral cathodic charge) vs.  $iR$  corrected potential derived from the pulse voltammetry measurement. **c**,  $C_{dl}$ -type capacitance derived from fitting the current profiles of the pulse voltammetry measurement.

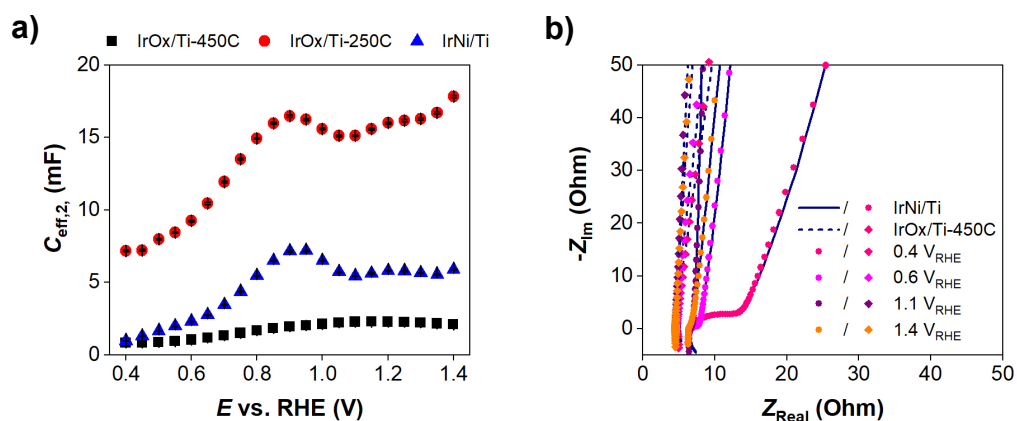
### Additional electrochemical assessments

To ensure the RDE measurements were not mass transport limited the rotation speed was varied; no dependence was observed (Supplementary Fig. 18). The effective capacitance derived from PEIS fitting of selected materials is shown in

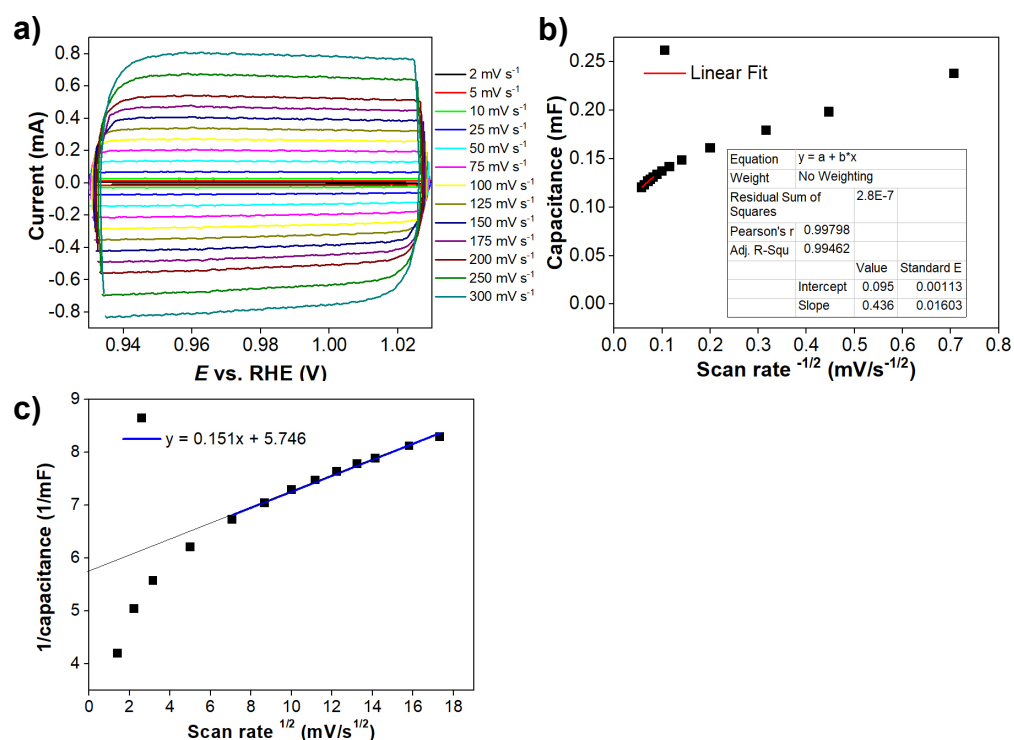
Supplementary Fig. 19 along with selected Nyquist plots. Voltammograms with different scan rates are shown together with evaluation of outer and total capacitance based on scan rate variation in Supplementary Fig. 20a.



**Supplementary Fig. 18 | Rotation speed dependent pulse voltammetry measurement using IrO<sub>x</sub>/Ti-250°C.** The results show the independence of the **a**, Tafel plot, **b**, total charge (integral cathodic charge) vs. *iR* corrected potential and **c**, total charge vs. log OER current to rotation speeds between 800 rpm and 2,000 rpm. Data in the manuscript employs 1,600 rpm.



**Supplementary Fig. 19 | Effective capacitance and Nyquist plots.** **a**, Effective capacitance (derived from PEIS fitting) as a function of potential. **b**, Example of selected impedance spectra (Nyquist plots) with the corresponding fits.

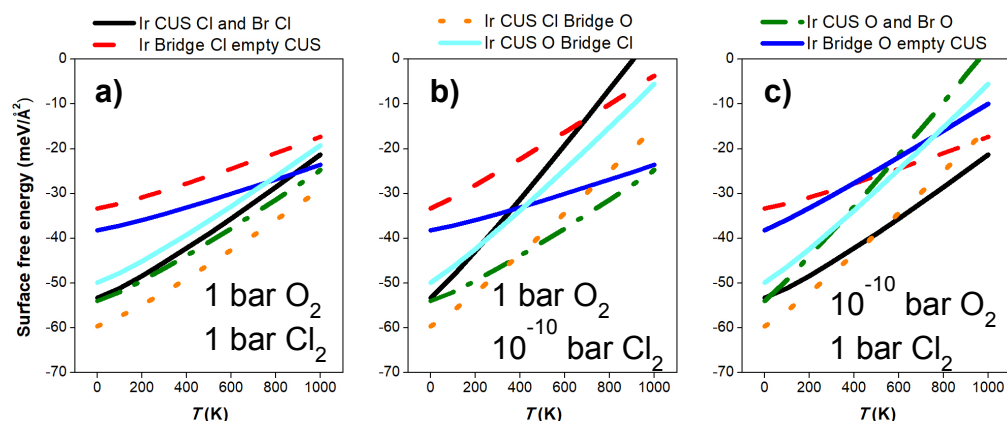


**Supplementary Fig. 20 | Voltammograms and outer/total capacitance.** **a**, *iR*-corrected cyclic voltammograms between 0.93 V and 1.03 V with different scan rates. **b**, and **c**, evaluation of outer and total capacitance based on scan rate variation experiments.

### Surface chlorination

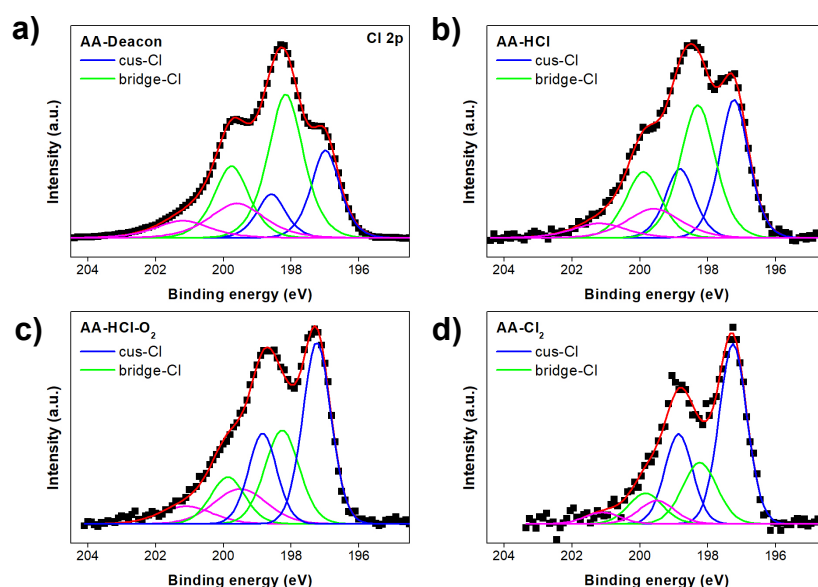
We showed the number of stored charges dominate the linear energy relationship mediating catalysis on crystalline iridium oxides by comparing DFT calculations on pure oxyhydroxide surfaces with those where O(H) was replaced by Cl. This choice was made as Cl is a non-reducible ligand that will only store one oxidative charge over the entire potential window of the OER<sup>29</sup> and thereby offers a means of further testing the importance of charge transfer. To verify this mechanism, we turned to experiment to irreversibly block surface sites with Cl.

We used ab initio atomistic thermodynamics to explore the competition between O and Cl binding on rutile-type IrO<sub>2</sub>, assuming Cl<sub>2</sub> and O<sub>2</sub> gas-phase sources. We found Cl tends to bind more strongly than O on the  $\mu_1$  site, see Supplementary Fig. 21. At non-zero Cl<sub>2</sub> pressure  $\mu_1$ -Cl is favored over  $\mu_1$ -O at low temperatures. Conversely, bridging  $\mu_2$ -O tends to be favored over bridging  $\mu_2$ -Cl except in the case of relatively high Cl chemical potential. These results suggest pure  $\mu_2$  chlorination is unlikely to be achieved, though the  $\mu_2$  to  $\mu_1$  ratio can be controlled to a degree.



**Supplementary Fig. 21 | Surface free energies O/Cl surface terminations.** Terminations on the (110) surface of rutile-type  $\text{IrO}_2$  are as indicated.

Our DFT studies suggest Cl can displace both  $\mu_1\text{-O}$  and  $\mu_2\text{-O}$  on rutile-type  $\text{IrO}_2$  (Supplementary Fig. 21). Thus, we treated an amorphous  $\text{IrO}_x$  powder in the Deacon reaction<sup>29</sup> and compared its OER activity before and after Deacon treatment. While the sample underwent massive deactivation upon the Deacon treatment (sample AA-D in Supplementary Fig. 9d), the reasons are not clear. Comparison of an AA-D electrode before and after OER by laboratory XPS shows most of the Cl 2p intensity is conserved after OER (Supplementary Fig. 22a), but detailed characterizations also indicate the Deacon treatment leads to crystallization (Supplementary Fig. 9c) and loss of BET surface area ( $36.46$  to  $22.84 \text{ m}^2 \text{ g}^{-1}$ ).



**Supplementary Fig. 22 | Cl 2p spectra of four chlorinated samples.** **a**, pristine Alfa-Aesar  $\text{IrO}_x$  treated in the Deacon reaction. **b**, AA-HCl: calcined Alfa-Aesar  $\text{IrO}_x$  sample treated in HCl at  $270 \text{ }^\circ\text{C}$ . **c**, AA-HCl- $\text{O}_2$ : calcined Alfa-Aesar  $\text{IrO}_x$  sample treated in HCl at  $270 \text{ }^\circ\text{C}$  followed by treatment in  $\text{O}_2$  at  $300 \text{ }^\circ\text{C}$ . **d**, AA- $\text{Cl}_2$ : calcined sample after treatment in  $\text{Cl}_2$  at RT. Photon energy:  $415 \text{ eV}$ .

We sought to disentangle the effects of surface chlorination from changes in surface area. To do so, the amorphous IrO<sub>x</sub> sample was first calcined in 1 bar air at 450°C, the highest temperature of the Deacon treatment. This calcination gave rise to crystallization (Supplementary Fig. 9c) and a reduction of the BET surface area (to 22.4 m<sup>2</sup> g<sup>-1</sup>). This loss in surface area led to a reduction of the OER activity (Supplementary Fig. 9d), but the sample (AA-450°C) was still significantly more active than the Deacon treated sample. Thus, we concluded the most important reason for deactivation of the Deacon treated sample was surface chlorination.

The significant degree of surface chlorination from the Deacon treatment makes it challenging to link the activity loss to charge storage, as the active sites may also be blocked. In the hope of finding a correlation between the degree of surface chlorination and the OER activity, we undertook a variety of treatments as summarized in Supplementary Tables 3 and 4 in the supplementary tables section. These include the pre-calcined (AA-450°C) sample under various chlorination conditions (in RT Cl<sub>2</sub>, in HCl at 270°C, and the HCl-270°C sample was also post-treated in O<sub>2</sub> at 300 °C). These samples show varying degrees of deactivation (Supplementary Fig. 9d) and surface chlorination (Supplementary Table 6 in the supplementary tables section). We concluded that increasing chlorination leads to continuous deactivation through site blocking and a reduction in oxidative charge storage, in agreement with our DFT results shown in Fig. 4 of the main text.

## Supplementary tables

**Supplementary Table 1 | Capacitance values of selected Ir samples.** The evaluation methods are indicated. All values in mF.

Method	Type	IrO <sub>x</sub> /Ti-250°C	IrNi/Ti	AA-IrO <sub>x</sub>	IrO <sub>2</sub> /Ti-450°C	AA-D
PV <sup>a</sup> $E_1 = 0.75$ V	total	19.7	7.4	5.5	2.8	0.35
PV <sup>b</sup> $E_1 = 1.35$ V	total	22.1/ 15.9 <sup>f</sup>	9.3/ 7.1 <sup>f</sup>	5.2/ 1.8 <sup>f</sup>	2.7/ 2.4 <sup>f</sup>	0.27/ 0.08 <sup>f</sup>
Line shape <sup>c</sup>	dl <sup>g</sup>	16-19	5.2-6.5	2.5-3.7	2.1-2.3	0.09-0.12
Scan rate <sup>d</sup>	total	17.9	5.4	3.6	2.3	0.19
Scan rate <sup>d</sup>	outer	6.5	3.53	1.7	1.9	0.12
EIS <sup>e</sup>	dl <sup>g</sup>	7.3-17.7 <sup>e</sup>	5.5-7.2 <sup>e</sup>	n.d.	1.1-2.5 <sup>e</sup>	n.d.

<sup>a</sup> PV integration with  $E_1 = 0.75$  V.

<sup>b</sup> PV integration with  $E_1 = 1.35$  V.

<sup>c</sup> Fit of cathodic line shape.

<sup>d</sup> Scan rate variation, see Supplementary Fig. 20.

<sup>e</sup> Fit EIS spectra, see Supplementary Fig. 19.

<sup>f</sup> First and second numbers correspond to the slopes of the total charge vs. potential curves before and after the potential the Tafel slope bends.

<sup>g</sup> Due to the much larger capacitance values as compared to the double layer capacitance of planar metallic electrodes, in reality we probe  $C_{dl}$ -type pseudocapacitance.

**Supplementary Table 2 | Areal capacitance values Alfa-Aeasar IrO<sub>x</sub>.** Evaluation methods for the Alfa-Aeasar based IrO<sub>x</sub> samples are indicated, values in  $\mu\text{F}/\text{cm}^2$ .

Evaluation method	Type of capacitance	AA-IrO <sub>x</sub>	AA-D
PV integration ( $E_1 = 0.75$ V)	total	1509	153
PV integration ( $E_1 = 1.35$ V)	total	1426/494 <sup>a</sup>	118/35 <sup>a</sup>
Fit cathodic line shape	dl <sup>b</sup>	686-1015	39-53
Scan rate variation	total	987	83
Scan rate variation	outer	466	53

<sup>a</sup> First and second numbers correspond to the slopes of the total charge vs. potential curves before and after the potential the Tafel slope bends.

<sup>b</sup> Due to the much larger capacitance values as compared to the double layer capacitance of planar metallic electrodes, in reality we probe  $C_{dl}$ -type pseudocapacitance.

**Supplementary Table 3 | Samples and chlorination treatments.** The listed samples and treatments were used in the chlorination study.

Sample	Treatment / #	Feed composition / vol.%	Treatment $T$ / K	BET / $\text{m}^2 \text{g}^{-1}$
Alfa Aesar IrO <sub>x</sub>	–	–	–	36.46
AA-D	Deacon <sup>a</sup>	HCl:O <sub>2</sub> :He = 10:20:70	723-623	22.84
AA-450 °C	Calcination	O <sub>2</sub> :N <sub>2</sub> = 21:79	723	22.40
AA-HCl <sup>b</sup>	Chlorination 1	HCl:He = 10:90	543	19.64
AA-HCl-O <sub>2</sub> <sup>b</sup>	Chlorination 2 <sup>c</sup>	a) HCl:He = 10:90	543	25.87
		b) O <sub>2</sub> :He = 20:80	573	
AA-Cl <sub>2</sub> <sup>b</sup>	Chlorination 3	Cl <sub>2</sub> :He = 10:90	298	22.02

<sup>a</sup> The sample was exposed for a total time of 3 h. <sup>b</sup> Chlorination treatments 1/2/3 were carried out after calcination at 723 K. <sup>c</sup> Each sub-treatment (a,b) was performed for 1.5 h.

**Supplementary Table 4 | Charge values during pulse voltammetry.** The broad potential window of 0.95 V to 1.7 V (non *iR*-corrected) was used. Cathodic potential: 0.75 V. Two samples (IrNi/Ti and IrO<sub>x</sub>/Ti-250°C) are selected to show that the cathodic and anodic charge is equal below the OER onset.

Non <i>iR</i> - corrected anodic potential / V	Charge (mC)			
	IrNi/Ti		IrO <sub>x</sub> /Ti-250°C	
	anodic	cathodic	anodic	cathodic
1.7	282.1	-5.93	320	-15.35
1.6	103.2	-5.73	130.63	-14.8
1.55	38.4	-5.5	57.52	-14.25
1.4	4.23	-4.1	10.58	-10.56
1.1	2.2	-2.19	5.44	-5.44
0.95	1.25	-1.26	3.09	-3.09

**Supplementary Table 5 | Cl<sub>2</sub> yield in Deacon reaction.** The yield for Alfa Aesar IrO<sub>x</sub> treatment at various temperatures. The collected sample was denoted as AA-D.

Order / #	Temperature <sup>a</sup> / K	Yield of Cl <sub>2</sub> / %
1	723	70.7
2	673	30.7
3	623	3.1

<sup>a</sup> Other conditions:  $F_T:W_{\text{samp}} = 40 \text{ L STP h}^{-1} \text{ g}_{\text{samp}}^{-1}$ , 10 vol.% HCl, O<sub>2</sub>:HCl = 2,  $P = 1 \text{ bar}$ ,  $t_h = 3 \text{ h}$ .

**Supplementary Table 6 | XPS results on surface chlorination.**

Sample	Cl/Ir ratio	Bridge Cl %	Cl(Bridge)/Ir
AA-450°C	0	–	0
AA-Cl <sub>2</sub>	0.076	26.7	0.02
AA-HCl-O <sub>2</sub>	0.48	31.6	0.152
AA-HCl	0.61	45.4	0.277
AA-D	0.62	53.4	0.331

**Supplementary Table 7 | Surfaces for minimum energy path calculations.  $E_a$  given in eV.**

$\mu_2$ sites	$\mu_1$ sites	$E_a$ Constant bias (pzc)	$E_a$ Constant charge	$E_a$ No solvent
OH/O	OH/O	0.78	0.88	0.41
O/O	OH/O	0.63	0.67	0.54
O/O	O/O	0.23	0.26	0.36
Cl/O	OH/O	–	0.94	0.83
Cl/O	Cl/O	–	1.03	0.50
Cl/O	O/O	–	0.62	–
O/O <sup>a</sup>	OH/7O <sup>a</sup>	–	0.40 <sup>a</sup>	–

<sup>a</sup> A (2×4) cell was used.

## References

1. Nong, H. N., Gan, L., Willinger, E., Teschner, D. & Strasser, P. IrO<sub>x</sub> core-shell nanocatalysts for cost- and energy-efficient electrochemical water splitting. *Chem. Sci.* **5**, 2955–2963 (2014).
2. Nong, H. N. *et al.* A unique oxygen ligand environment facilitates water oxidation in hole-doped IrNiO<sub>x</sub> core-shell electrocatalysts. *Nat. Catal.* **1**, 841–851 (2018).
3. Reier, T. *et al.* Electrocatalytic oxygen evolution on iridium oxide: Uncovering catalyst-substrate interactions and active iridium oxide species. *J. Electrochem. Soc.* **161**, 876–882 (2014).
4. Ardizzone, S., Fregonara, G. & Trasatti, S. “Inner” and “outer” active surface of RuO<sub>2</sub> electrodes. *Electrochim. Acta* **35**, 263–267 (1990).
5. De Pauli, C. P. & Trasatti, S. Electrochemical surface characterization of IrO<sub>2</sub> + SnO<sub>2</sub> mixed oxide electrocatalysts. *J. Electroanal. Chem.* **396**, 161–168 (1995).
6. Li, G., Anderson, L., Chen, Y., Pan, M. & Abel Chuang, P.-Y. New insights into evaluating catalyst activity and stability for oxygen evolution reactions in alkaline media. *Sustain. Energy Fuels* **2**, 237–251 (2018).
7. Lassali, T. A. F., Boodts, J. F. C. & Bulhões, L. O. S. Charging processes and electrocatalytic properties of IrO<sub>2</sub>/TiO<sub>2</sub>/SnO<sub>2</sub> oxide films investigated by in situ AC impedance measurements. *Electrochim. Acta* **44**, 4203–4216 (1999).
8. Rasten, E., Hagen, G. & Tunold, R. Electrocatalysis in water electrolysis with solid polymer electrolyte. *Electrochim. Acta* **48**, 3945–3952 (2003).
9. Orazem, M. *et al.* Dielectric properties of materials showing constant-phase-element (CPE) impedance response. *J. Electrochem. Soc.* **160**, C215–C225 (2013).
10. Pfeifer, V. *et al.* In situ observation of reactive oxygen species forming on oxygen-evolving iridium surfaces. *Chem. Sci.* **8**, 2143–2149 (2017).

11. Zichittella, G., Aellen, N., Paunović, V., Amrute, A. P. & Pérez-Ramírez, J. Olefins from natural gas by oxychlorination. *Angew. Chemie Int. Ed.* **56**, 13670–13674 (2017).
12. Yeh, J. J. & Lindau, I. Atomic subshell photoionization cross sections and asymmetry parameters:  $1 \leq Z \leq 103$ . *At. Data Nucl. Data Tables* **32**, 1–155 (1985).
13. Giannozzi, P. *et al.* QUANTUM ESPRESSO: a modular and open-source software project for quantum simulations of materials. *J. Phys. Condens. Matter* **21**, 395502 (2009).
14. Gianluca Prandini, Antimo Marrazzo, Ivano E. Castelli, Nicolas Mounet, N. M. A Standard Solid State Pseudopotentials (SSSP) library optimized for precision and efficiency (Version 1.1, data download). *Mater. Cloud Arch.* doi: 10.24435/materialscloud:2018.0001/v3 (2018).
15. Dal Corso, A. Pseudopotentials periodic table: From H to Pu. *Comput. Mater. Sci.* **95**, 337–350 (2014).
16. Marzari, N., Vanderbilt, D., De Vita, A. & Payne, M. C. Thermal contraction and disordering of the Al(110) surface. *Phys. Rev. Lett.* **82**, 3296–3299 (1999).
17. Nørskov, J. K. *et al.* Origin of the overpotential for oxygen reduction at a fuel-cell cathode. *J. Phys. Chem. B* **108**, 17886–17892 (2004).
18. Limmer, D. T., Willard, A. P., Madden, P. & Chandler, D. Hydration of metal surfaces can be dynamically heterogeneous and hydrophobic. *Proc. Natl. Acad. Sci.* **110**, 4200–4205 (2013).
19. Wang, D., Sheng, T., Chen, J., Wang, H.-F. & Hu, P. Identifying the key obstacle in photocatalytic oxygen evolution on rutile TiO<sub>2</sub>. *Nat. Catal.* **1**, 291–299 (2018).
20. Gauthier, J. A., Dickens, C. F., Chen, L. D., Doyle, A. D. & Nørskov, J. K. Solvation effects for oxygen evolution reaction catalysis on IrO<sub>2</sub>(110). *J. Phys. Chem. C* **121**, 11455–11463 (2017).

21. Otani, M. & Sugino, O. First-principles calculations of charged surfaces and interfaces: A plane-wave nonrepeated slab approach. *Phys. Rev. B* **73**, 115407 (2006).
22. Bonnet, N., Morishita, T., Sugino, O. & Otani, M. First-principles molecular dynamics at a constant electrode potential. *Phys. Rev. Lett.* **109**, 266101 (2012).
23. Dupont, M. F. & Donne, S. W. Charge storage mechanisms in electrochemical capacitors: Effects of electrode properties on performance. *J. Power Sources* **326**, 613–623 (2016).
24. Bard, A. J. & Faulkner, L. R. *Electrochemical methods - fundamentals and applications*. (John Wiley & Sons, Inc., 2000).
25. Fierro, S., Nagel, T., Baltruschat, H. & Comninellis, C. Investigation of the oxygen evolution reaction on Ti/IrO<sub>2</sub> electrodes using isotope labelling and on-line mass spectrometry. *Electrochem. commun.* **9**, 1969–1974 (2007).
26. Clancy, J. P. *et al.* Spin-orbit coupling in iridium-based 5d compounds probed by X-ray absorption spectroscopy. *Phys. Rev. B* **86**, 195131 (2012).
27. Schmickler, W. & Santos, E. *Interfacial Electrochemistry*. (Springer, 2010). doi:10.1007/978-3-642-04937-8
28. Teschner, D. *et al.* In situ surface coverage analysis of RuO<sub>2</sub>-catalysed HCl oxidation reveals the entropic origin of compensation in heterogeneous catalysis. *Nat. Chem.* **4**, (2012).
29. Teschner, D. *et al.* An integrated approach to Deacon chemistry on RuO<sub>2</sub>-based catalysts. *J. Catal.* **285**, 273–284 (2012).